

GUSTAVUS ADOLPHUS COLLEGE

Petrologic Investigation of a Graphitic Breccia Pipe in Proximity to the Tamarack Cu-Ni-PGE Deposit; Carlton County, Minnesota

*A description of mineralogy and chemistry to delineate the relationship between intrusion
and breccia*

MICHAEL HENDRICKSON

5/23/2011

A thesis submitted in partial fulfillment of the requirements for the degree of
Bachelor of Arts
(Geology)
At
Gustavus Adolphus College
2011

Abstract:

Breccia pipe formation is commonly associated with ore deposits, and just as commonly the relationship between breccia formation and ore deposit emplacement is unknown. As breccia pipe mineralogy can be applied to making a connection to the ore-hosting rock, this study delineates primary and alteration mineral assemblages of a breccia matrix in order to define the material source. This relates the adjacent ore-hosting intrusion to the breccia pipe and is used to determine which came first and provides data for a time-space model of emplacement.

Prior to this investigation, Rio Tinto Corporation intercepted a breccia pipe adjacent to the Tamarack Cu-Ni-PGE deposit in north central Minnesota. The Tamarack Intrusion is mafic and composed of two discrete rock units: a lower coarse grained feldspathic Iherzolite and an upper medium grained Iherzolite, both derived from the same source. In map view the Tamarack Intrusion is tadpole shaped, and surrounded by variable amounts of what was once melted country rock, but is now crystallized igneous rock. The breccia pipe is adjacent to a portion of the intrusion containing a large amount of this type of igneous rock. The breccia is characterized by variably sized graphitic clasts set in a highly altered matrix composed mainly of clays, sericite and chlorite, and contacts the end-of-hole igneous rocks (melted country rocks) of the intrusion sidewall or cupola. Petrographic analysis of the breccia matrix yields relatively large amounts of felsic mineralogies. Compared to the petrology and chemistry of the Tamarack Intrusion, the breccia matrix more closely resembles the end-of-hole igneous rocks (melted country rocks). Being that these melted country rocks are a secondary result of the Tamarack Intrusion, the breccia matrix chemistry constrains a syntectonic model for the breccia and intrusion.

Acknowledgements

I extend a great deal of gratitude towards James Welsh, Elizabeth Goeke, Julie Bartley, and Laura Triplett for their aid in the completion of this study. I would also like to thank Dean Rossell, Brian Goldner and Rio Tinto Corporation for their contribution of real time data and information, and Dean again for suggesting the project. Lastly, I would like to thank Jeff Thole of Macalester College, whose analytical advice was paramount. Without these contributors this study would not have been possible.

Table of Contents

Abstract.....	1
Acknowledgments.....	2
Table of Contents.....	3
List of Figures.....	4
Introduction.....	5
Geologic Setting.....	7
Geology of the Tamarack.....	13
Previous Work.....	14
Methods.....	15
Results	16
Discussion.....	25
Conclusion.....	32
References Cited.....	34
Appendix.....	36

List of Figures

1.) Regional Geology.....	7
2.) Local Geology.....	7
3.) Timeline of tectonic events.....	12
4.) Geophysical map of the Tamarack.....	14
5.) Schematic cross section of the Tamarack.....	14
6.) Schematic representation of the Breccia Pipe.....	19
7.) Photos of thin sections representing the Breccia.....	20
8.) Photos of core.....	21
9.) Photomicrographs of igneous textures in breccia matrix.....	22
10.) QAP classification of end-of-hole igneous rocks	23
11.) Breccia matrix mineralogy.....	24
12.) Mineral reactions.....	27
13.) Proposed model of breccia pipe formation.....	30
14.) Plan view of Tamarack showing cross section lines.....	31
15.) Hypothetical cross section of breccia pipe and Tamarack intrusion.....	32

Introduction

Layered mafic intrusions (LMI) host in excess of 85% of the platinum-group-element (PGE), 80% of the chromium, 60% of the vanadium, and 40% of the nickel reserves of the Earth's crust (Hutchinson, 1983). Many of the processes and parameters considered prerequisite to economic concentrations of these metals in LMIs are unresolved and include thermodynamic constraints, convective magma flow, and the chemical and physical quantification of multiple magma pulses. Hence, deposit-scale descriptions of petrology and chemistry are used in the context of regional geology to delineate source, transport, and trap of precious and base metals. The deposit scale structure and chemistry can be linked to specific tectonic events, thus constraining space-time economic mineralization. Breccia pipes are critical parts of deposit scale description, as they aid to spatially constrain periods of energy change relative to quantitatively dated tectonic events. The breccia pipe may serve as a spatial marker of exceeding the maximum amount of energy a system can absorb, and its relative age relationship to economic deposits constrains the timing of mineralization to before or after (Hronsky, 2011). Such constraint then aids in describing the duration and continuity of base and precious metal mineralization within LMIs.

As a result of rising demand for metals, the Duluth Complex of northeastern Minnesota has become internationally recognized for hosting copper-nickel-platinum group element (Cu-Ni-PGE) deposits. However, it is less well known that a number of smaller mafic intrusions of the same age exist outside the defined boundaries of this suite of rocks and have the potential to host economic concentrations of these metals. A breccia pipe located along the boundary of Carlton and Aitkin counties, near the town of Tamarack

in northern Minnesota, is related to such an intrusion, aptly named the Tamarack Intrusion (Figure 1 and 2)(Goldner, 2011). The Tamarack Intrusion was discovered by Rio Tinto Corporation, and its formation process is being evaluated in order to determine its economic potential. Although not economically mineralized, the breccia pipe provides potential insight for understanding deposit-scale processes as mentioned above.

The Tamarack Intrusion and associated breccia pipe intrude the Paleoproterozoic Thomson Formation, a sulfidic-graphitic metasedimentary unit in the Animikie Basin (Boerboom, 2009). This study describes a core intercepting the breccia pipe and twenty associated thin sections representing relevant parts of the breccia as well as the chemical composition of the breccia matrix derived from Scanning Electron Microscope with Energy Dispersive Spectrometry (SEM-EDS). These data are compared to published chemical and petrologic data from the Tamarack in order to deduce a chemical and textural relationship and to establish the order of events during the emplacement of the Tamarack Intrusion.

Geologic Setting

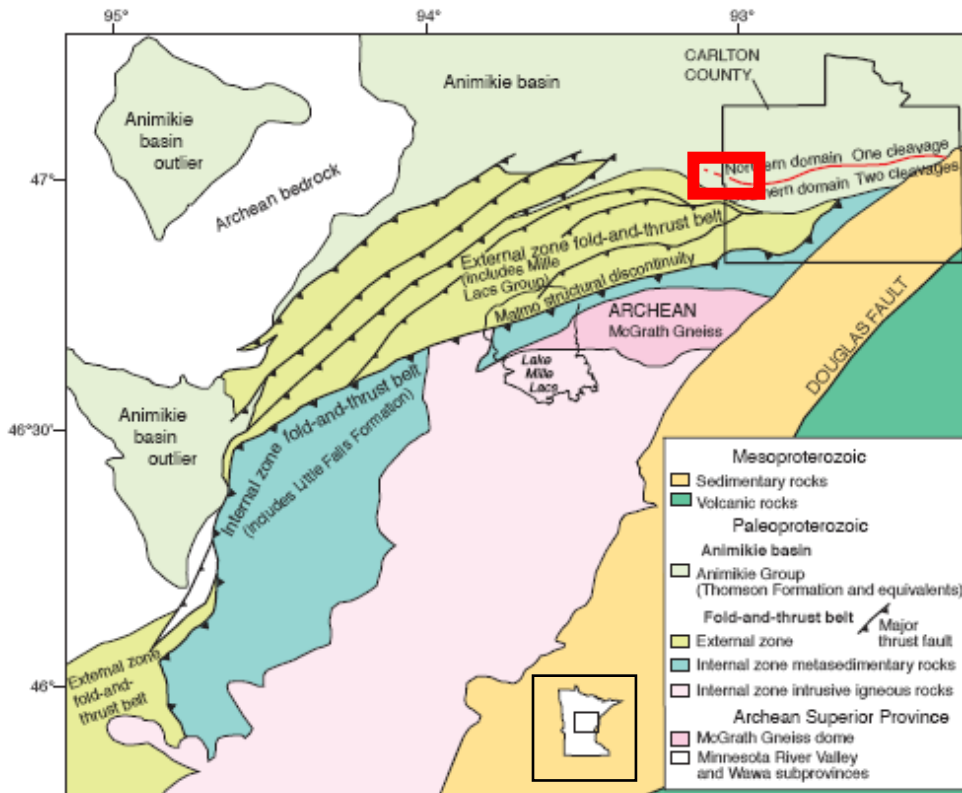


Figure 1: Large scale geologic representation of Carlton County and surrounding region. Carlton County outlined in black. **Figure 2** is outlined in red and expanded below. Modified from Boerboom (2009).

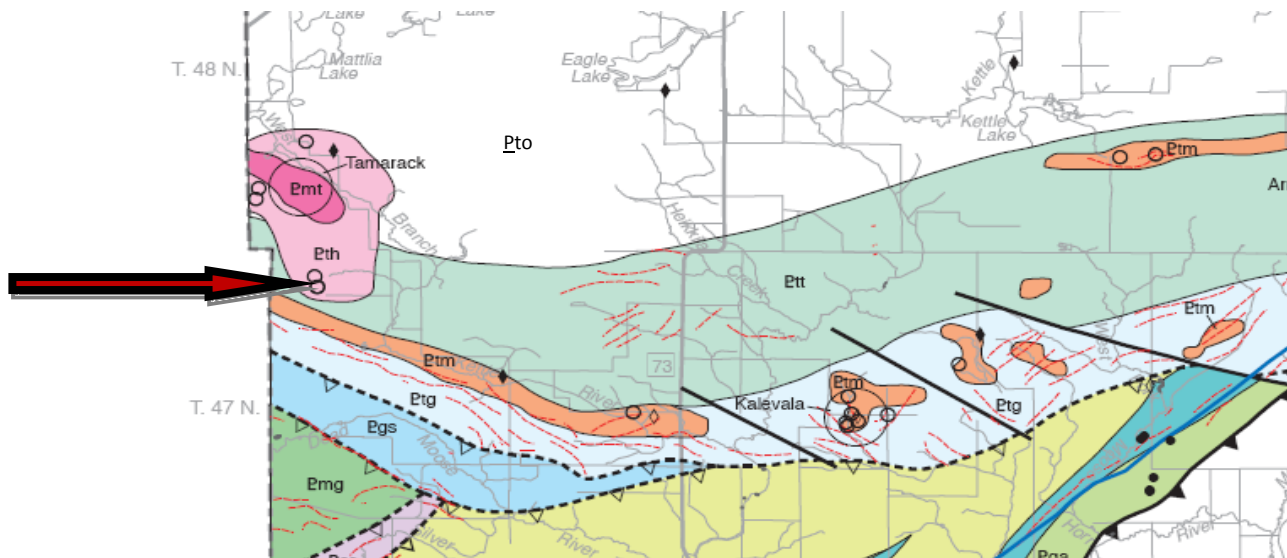


Figure 2: Expanded from Figure 1. The Tamarack Intrusion is represented by dark pink (Pmt) and its associated aureole by light pink (Pth). The arrow indicates the location of the drill hole intercepting the breccia pipe. White, light green, orange, and light blue Thompson Formation rock units (Pto, Ptt, Ptm, Ptg) surround the Tamarack Intrusion. Modified from Boerboom (2009).

Tectonic Setting and Regional Structure

The regional geologic setting is shown in Figure 1; the location of the study area is outlined in red. The Animikie Basin is the northernmost suite of rocks on the map, and comprises slate, metagreywacke, and chert. Immediately truncating the Animikie Basin to the south is the External Zone fold-and-thrust belt, a set of imbricate thrust sheets, which includes the Mille Lacs Group generally comprising phyllite, schist, slate, metagreywacke, metagabbro, metadiabase, and metabasalt. The Internal Zone fold-and-thrust belt is south and adjacent to the External zone fold and thrust belt and comprises slate, metagreywacke, and intrusive igneous rocks (Boerboom, 2009). The Duluth Complex is located northeast of the study area, comprises a suite of bi-modal tholeiitic rocks, and is the result of the Mid-continent Rift System (MRS) mantle-plume initiated event at ~1100 Ma (Vervoort et al, 2007). A structural discontinuity separates the External Zone fold-and-thrust belt from the Animikie Basin, and the Malmo Discontinuity separates the External Zone fold-and-thrust belt from the Internal Zone fold-and-thrust belt (Boerboom, 2009).

Animikie Basin Geology

The Paleoproterozoic Animikie Basin Sequence comprises the lowermost Pokegama Quartzite, overlain by Biwabik Iron Formation, which is in turn overlain by the Virginia, Rove and Thomson formations (Chandler et. al., 2007). The Thomson Formation is the most relevant to this study, as it is locally intruded by the Tamarack Intrusion within the study area.

Thomson Formation rock units (P_{tt} and P_{to}, Figure 2) of the Animikie Basin generally consist of meta-greywacke and slate. Unit P_{to} of the Animikie Basin comprises gray, rhythmically interbedded argillite, siltstone, and greywacke metamorphosed under

lower greenschist facies conditions. Strata are folded to upright and open, and regional folding produced subvertical axial planar slaty cleavage. Graywacke beds locally contain small pyrite cubes and zoned carbonate concretions that are generally six to ten inches, but may reach three feet in length, and are flattened along cleavage planes. Unit Ptt of the Animikie Basin is a gray, rhythmically interbedded argillite, siltstone, and greywacke with bedding-parallel metamorphic foliation cut by a nearly vertical crenulation cleavage associated with upright folds with axes that are oriented similar to fold axes in the unit Pto. It possesses locally strong carbonaceous and/or graphitic lenses and scattered to abundant pyrite cubes (Boerboom, 2009).

Tectonic Evolution

Regional deformation in Carlton County is primarily the result of the Penokean Orogeny (~1890 Ma) (Holm et al, 2007). Isotopic dating and structural evidence for the Yavapai and Mazatzal orogenies is present, but the paucity of observed fabric distortions in the rock hosting the Tamarack Intrusion and reset argon isotope dates of mica and amphibole in the same country rock suggests that these younger orogenies did not substantially affect the study area (Van Schmus et al, 2007). The observed geology is the result of a complex history of continental accretion, aborted rifting, and resultant sedimentation and metamorphism.

Relevant tectonic history begins with the Penokean Orogeny (~1890 Ma), that is characterized by development of a south-facing continental margin (Figure 3). The Pembine-Wausau island arc complex and the Marshfield micro-continent collided with the Superior margin 1880-1850Ma (Vervoort et al., 2007). The resultant fold-and-thrust belt (Figure 1) is composed of variably deformed volcanic and sedimentary rock, mostly

metamorphosed to greenschist facies. Truncating this feature to the south is the Malmo Discontinuity, a major south-dipping thrust fault also attributed to the Penokean Orogeny. Concurrently with and post-dating Penokean structures, one or more foreland basins were produced as a result of tectonic loading; the Animikie Basin is the most prominent of these Paleoproterozoic foreland basins. Deposition of sediment in the Animikie Basin was episodic, and is thought to have taken place synchronously with and after the Penokean Orogeny, allowing these sediments to be metamorphosed to greenschist facies as a result of tectonic pressure during deposition (Schulz et al, 2007) (Figure 3). This suite of metasediments is composed of the basal Pokegama Quartzite, overlain by the Biwabik Iron Formation, and capped by a sequence of fine clastics known as the Thompson, Virginia, and Rove formations (Chandler et. al., 2007). Following this activity the Yavapai Orogeny (1800-1720 Ma) and Mazatzal Orogeny (1700-1600 Ma) occurred, accreting terrain to the south of the study area, as well as imposing low-grade metamorphism on the Animikie Basin (Figure 3) (Schulz et al, 2007).

The MRS became active after these continent building episodes largely as a result of a mantle plume (Figure 3), which caused the emplacement of the Duluth Complex and related satellite intrusions into the Animikie Basin. MRS formation occurred in four stages: an early, latent, main, and late stage. The early stage volcanism occurred 1109-1106 Ma, and is characterized by reversed geomagnetic polarity. The latent stage took place 1106-1102 Ma, with dominantly rhyolitic volcanism, largely the result of mafic magma localized in the lower crust causing anatectic melting and transport of felsic magma to the surface. The main and most voluminous stage, occurs 1100-1096 Ma, displays normal polarity and produced a variety of rock types as a result of the rise of magma chambers and plume

intensity. The late stage took place 1094-1086 Ma and is characterized by composite volcanism as a result of decrease in volcanic activity as the plate drifted off the plume (Goldner, 2011). Overall, isotopic evidence suggests differing contributions from the lithosphere and asthenosphere. This tectonic activity and volcanism is the cause of the Tamarack Intrusion and related breccia pipe formation (Goldner, 2011).

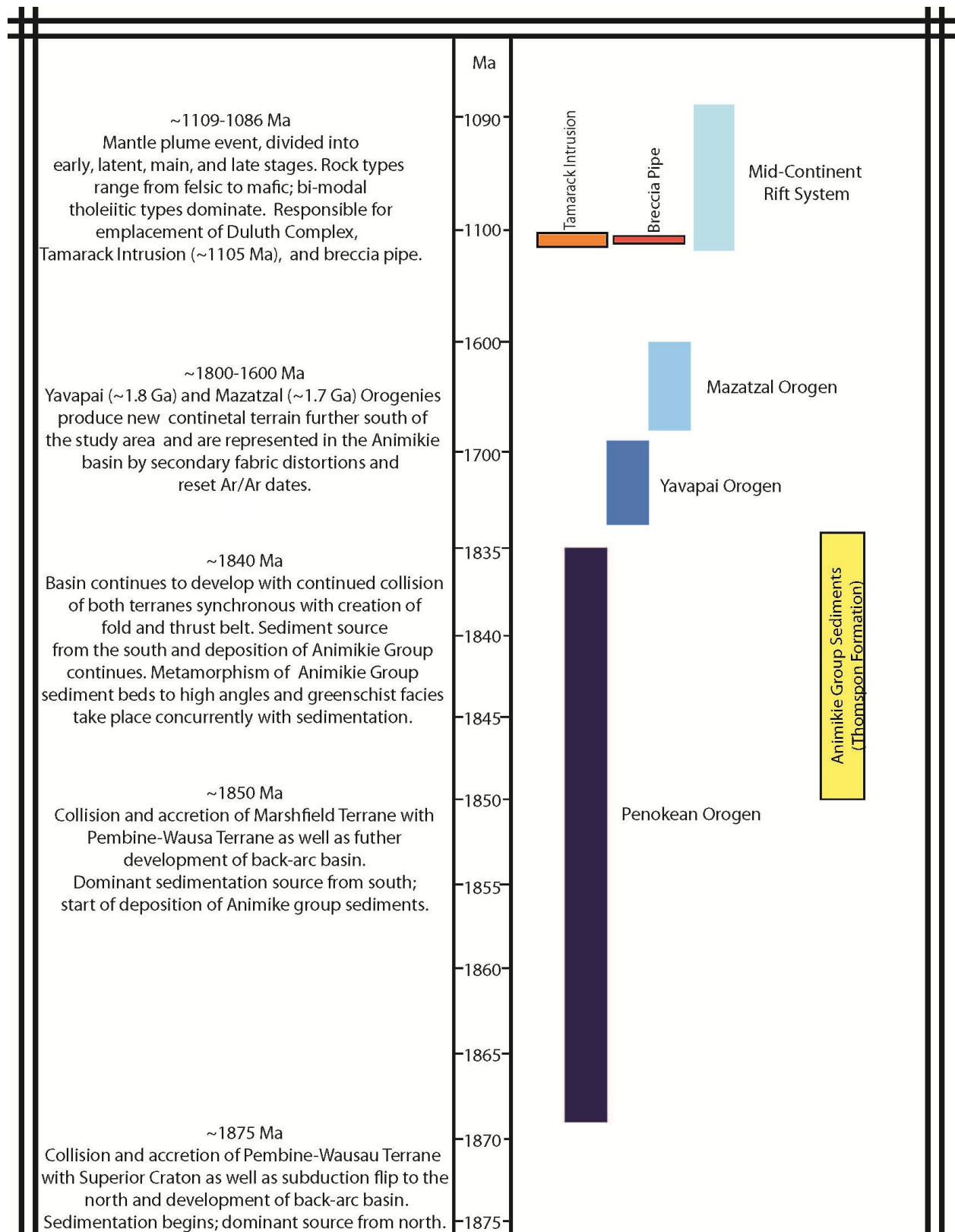


Figure 3: Time-correlated representation of important tectonic events, rock units, Tamarack Intrusion and breccia pipe formation. Dates taken from Shultz and Cannon (2007). Note that the time scale is not linear so as to easily demonstrate relationships between key events.

Geology of the Tamarack Intrusion

The Tamarack Intrusion and breccia pipe drill collar are shown in Figure 2. This Keweenawan (1100Ma) (Goldner, 2011) mafic intrusion intrudes the Paleoproterozoic Thomson Formation and is characterized by a tail, neck and bowl (Figure 4). The intrusion consists of a lower coarse-grained feldspathic lherzolite and an upper finer-grained lherzolite (Goldner, 2011) (Figure 5). The lower coarse-grained feldspathic lherzolite is composed of coarse olivine cumulates; the upper lherzolite is composed of relatively fine olivine mesocumulates to adcumulates. Consequently, the intrusion is attributed to two discrete emplacement phases by Goldner (2011), originating from the same magma source. The upper lherzolite unit is hypothesized to have intruded after emplacement of the lower coarse-grained feldspathic lherzolite unit, while the latter was still molten. Based on the composition of the basal chill margin within the lowermost feldspathic lherzolite unit, Goldner (2011) was able to deduce a parent magma composition by subtracting the compositional contribution of 30% olivine phenocrysts. The parent magma composition is interpreted to be a low Ti-P, high-MgO olivine tholeiite, with a Mg # of 68.5. This parent magma is very similar to other early phase and primitive MRS basalts of the Duluth Complex (Goldner, 2011). Given the smooth progression of evolved rock composition upward through the intrusion cross section, closed system crystal fractionation is inferred. In the bowl area of the intrusion, gabbro and granophyre gabbro form the distal portions of the intrusion; the latter formed from partial melting of country rock (Goldner, 2011).

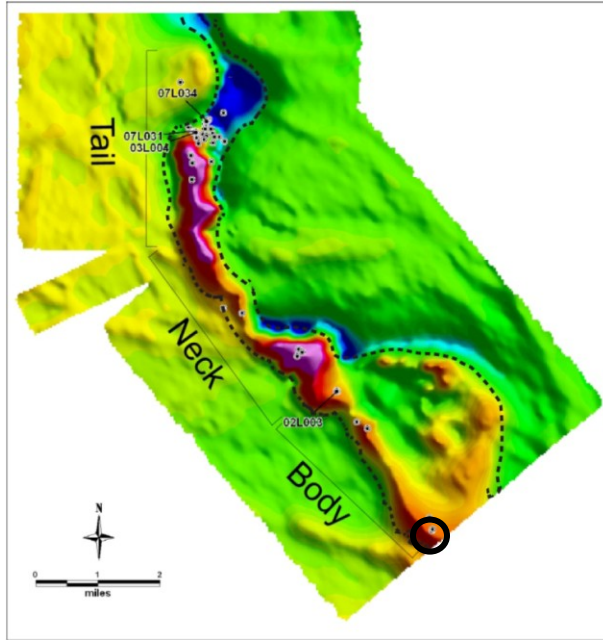


Figure 4: Aeromagnetic map of the Tamarack Intrusion with breccia intercepting drill collar outlined in black. Modified from Goldner (2011).

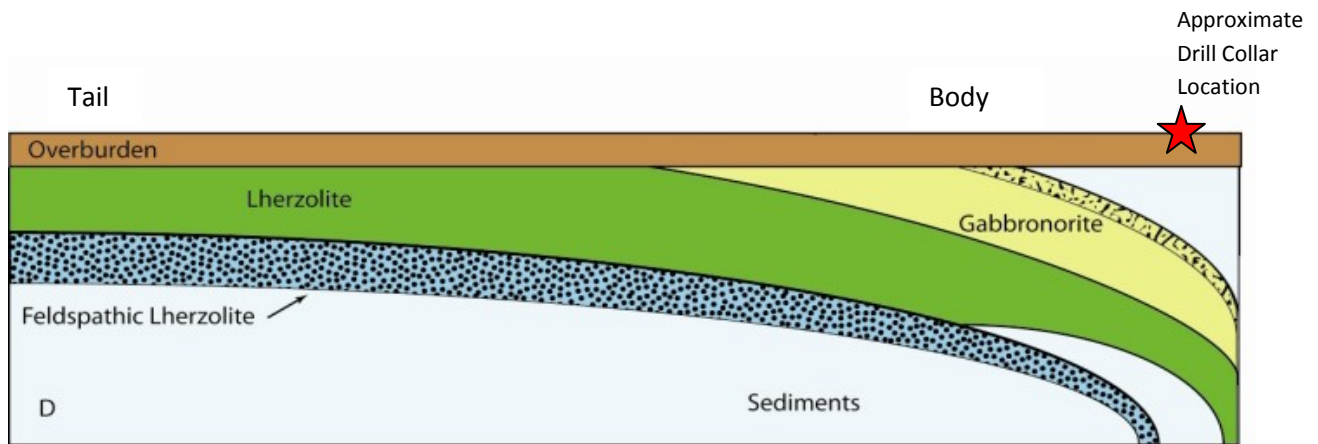


Figure 5: Schematic Cross Section of the Tamarack Intrusion. From Golder (2011).

Previous Work

The Precambrian Research Center has published extensively on the regional geology of the Duluth Complex and surrounding region (Precambrian Research Center Volume 157, 2007). As the name implies tectonic evolution intrusive events, sedimentation, and metamorphic events have been described for Minnesota, much of the Midwest, and Canada from the Archean to the initiation of the Cambrian. Most importantly, this volume

concludes much of the continental terrane previously attributed to the Penokean Orogeny is actually the result of the Yavapai and Mazatzal orogenies (Holm et al, 2007). In addition, the evolution of the MRS is described in detail, which enables time-correlation to the breccia producing Tamarack Intrusion. Boerboom (2009) has published a series of bedrock geologic maps of Carlton County, and Goldner (2011) provides a deposit-scale description of the Tamarack Cu-Ni-PGE deposit. Boerboom's (2009) bedrock geologic maps depict lithology and structure of Carlton County, as well as the eastern most portion of the Tamarack intrusion, all of which were mapped relying heavily on geophysics. The Tamarack is contained entirely within Thomson Formation based on these maps. Goldner's (2011) deposit scale description provides chemical compositions of the intrusion at various depths and locations in order to deduce intrusion evolution and economic significance. The emplacement of the Tamarack into the sulfidic Thomson Formation as depicted by Boerboom (2009), in conjunction with Goldner's (2011) deposit-scale description and coupled with regional geology indicate the Tamarack is synchronous with the early stage of mid-continent rifting.

Methods

The author created a lithologic reference frame by logging (Figure 6) and photographing (Figure 8) the breccia core. In addition, a suite of 20 thin sections (Figure 7) 1) sample the breccia and assimilated country rock and 2) sample anomalous areas within major lithologies and proximal lithologies, such as reaction rims and metasediments. Petrographic analysis was completed by point counting, and spacing of points was determined by crystal size. Most points were counted in breccia matrix and the end-of-hole

igneous rock. Sample sizes ranged from 700-2000 points on 27mm x 46 mm thin sections, and standard IUGS classification schemes (Le Maitre, 2002) were applied. SEM-EDS analysis was conducted at Macalester College in order to delineate chemical composition of the matrix, which was too fine grained to deduce by optical methods. Modal percentages of minerals derived by petrography are calculated in Microsoft Excel, and graphed on an IUGS ternary diagram (Figure 10). SEM-EDS derived weight percent of elements are qualitative; only relative abundances of elements are combined to represent mineral phases (Figure 11) (Appendix D). Alteration minerals observed in matrix are attributed to schematic reactions (Figure 12) using alteration mineral chemistry as a vector to qualitatively deduce likely primary minerals and thus a general primary rock type: felsic, mafic, or intermediate.

Results

Core, Hand and Thin Section

Figure 6-8 illustrate breccia pipe lithology and general thin section morphology. The core log (Figure 6) provides a general representation of differences in breccia alteration and lithologic breaks. Figure 7 demonstrates variation in breccia matrix alteration, and clast size and distribution. Figure 8 depicts hand sample appearance. For more detailed rock descriptions, see the written core log and thin section descriptions (Appendix A and Appendix B). Although the breccia is not intercepted continuously, it is intercepted by the drill hole for approximately 160 meters, from 65 to 225 meters below surface. Given the oblique drill angle to the breccia pipe a continuous breccia is not delineated, but likely (Figure 15). Metasediment (Thomson Formation) was intercepted for approximately 75 meters, from 140 to 215 meters below surface, and is intermittently truncated by breccia material. The end-of-hole igneous rock grades to higher felsic mineralogy up-section

(monzogabbro→granodiorite→ monzogranite) (Figure 10) and was sampled continuously from approximately 225 meters to 257 meters (end of hole). The total thickness of this end-of-hole igneous rock approaches 30 m in this core, which is not necessarily representative of the unit as a whole.

In hand sample (Figure 6, 7 and 8), the breccia pipe is characterized by rounded to sub-rounded black graphite clasts set in a fine-grained, dark green, and non-foliated matrix. Clasts range in diameter from 5-50 mm and possess concentric foliations, with quartz being the most abundant mineral in the microlithons. Clasts comprise ~15 to 65% of the breccia intrusion. Matrix mineralogy was too fine to classify in hand sample or petrographically and is described below with detailed SEM-EDS data provided in Appendix D. Matrix alteration intensity varies widely throughout section from partial preservation of igneous texture to complete obliteration of igneous texture. Point counts and normalized modal percentages of minerals in thin sections of end-of-hole igneous rocks are provided in Appendix C; photos of thin sections are provided in Figure 7. Sample L02-02-257 is classified as a quartz gabbro, L02-02-240 as a granodiorite, L02-02-231 as a monzogranite and L02-02-228 was too altered to classify (Figure 10). Grain size and modal percentages of quartz and K-feldspar increase up-section.

Fine-grained igneous textures most closely resembling, but still finer than sample L02-02-257, are well preserved in the breccia matrix in Samples L02-02-94, L02-02-183, and L02-02-191 (Figure 9 A,B,C). Alteration of the matrix is intense; the most common alteration minerals in matrix are clays (pyrophyllite?), sericite, chlorite, and amphibole. Pyrophyllite, clays and sericite are often indistinguishable in thin section; in optically

delineated mineral mode data tables (Appendix C) they are all classified as pyrophyllite. This ambiguity is partially addressed by SEM-EDS analysis as spectra of the breccia matrix provided in Appendix D yield relative abundance of potassium. Sericite can be distinguished from pyrophyllite and clays by this relative abundance. These data (Appendix C and D) imply clays, sericite, and/or pyrophyllite are the common alteration minerals in the breccia matrix. The only way to distinguish between pyrophyllite and the various clays present is by x-ray diffraction analysis.

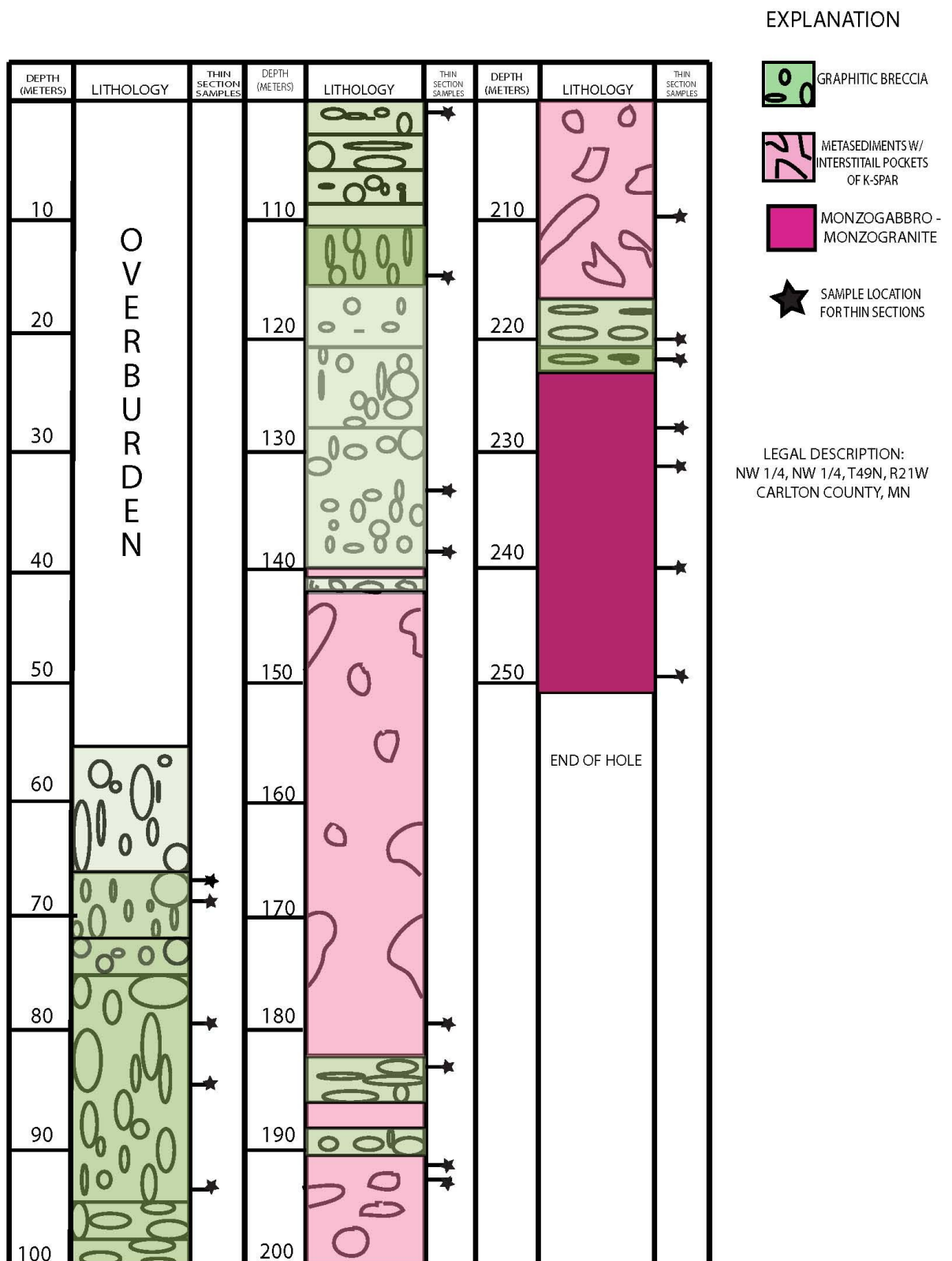


FIGURE 6: Core log (hole L02-02) of breccia pipe. See written core log in Appendix A for detailed description of lithologic breaks. Light shades of green indicate intense alteration of the breccia matrix, darker shades of green indicate less intense alteration of the breccia matrix. This core log is for schematic purposes only.

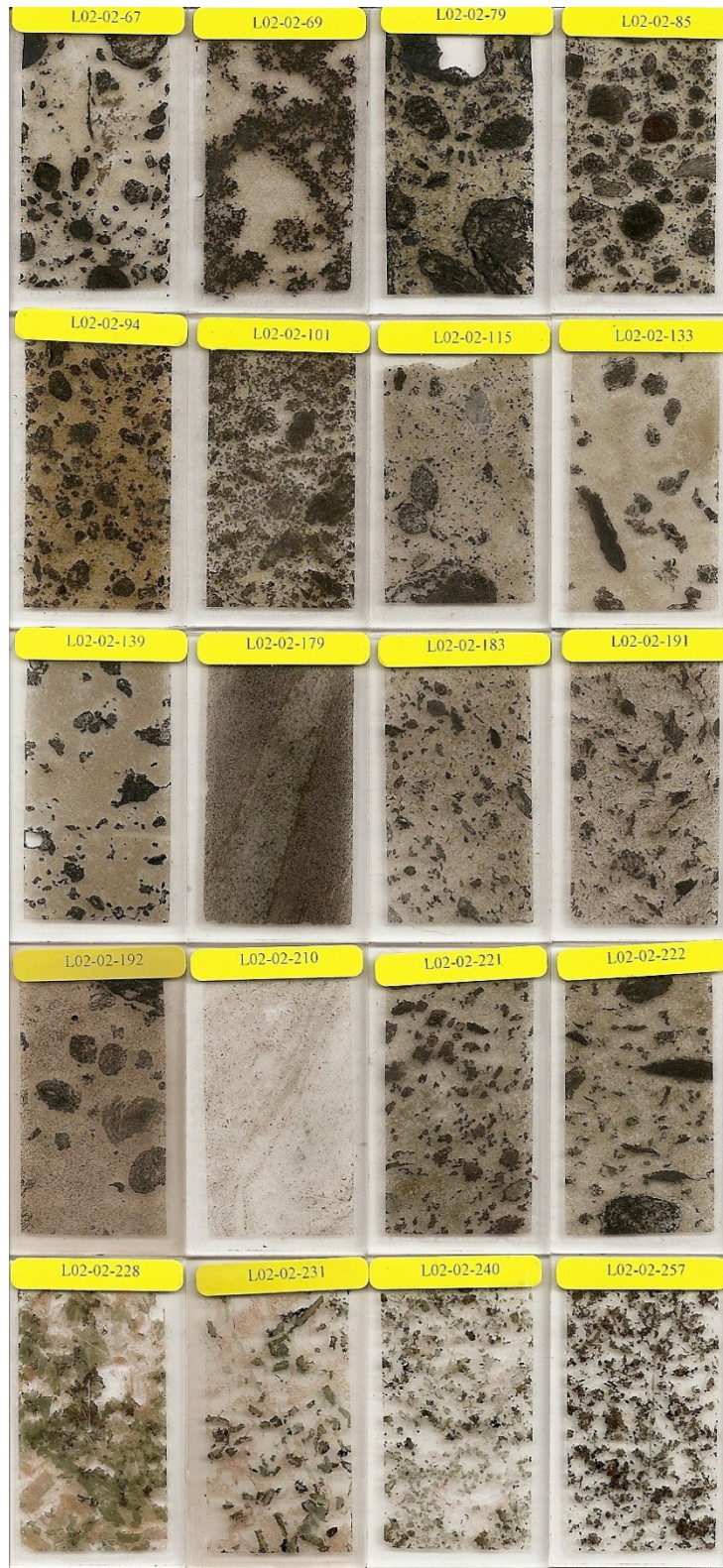


Figure 7: Photos of thin sections taken from specified locations in Figure 6, last digits signify depth in meters.



A



B



C



D



E



F



G



H

Figure 8: Photos of breccia pipe: A, B, F breccia; C graphite-rich breccia; D, E metamorphosed sediment; G breccia and metasediment with interstitial pockets of K-feldspar; H quartz gabbro-monzogranite at base of hole (melted metasediments).

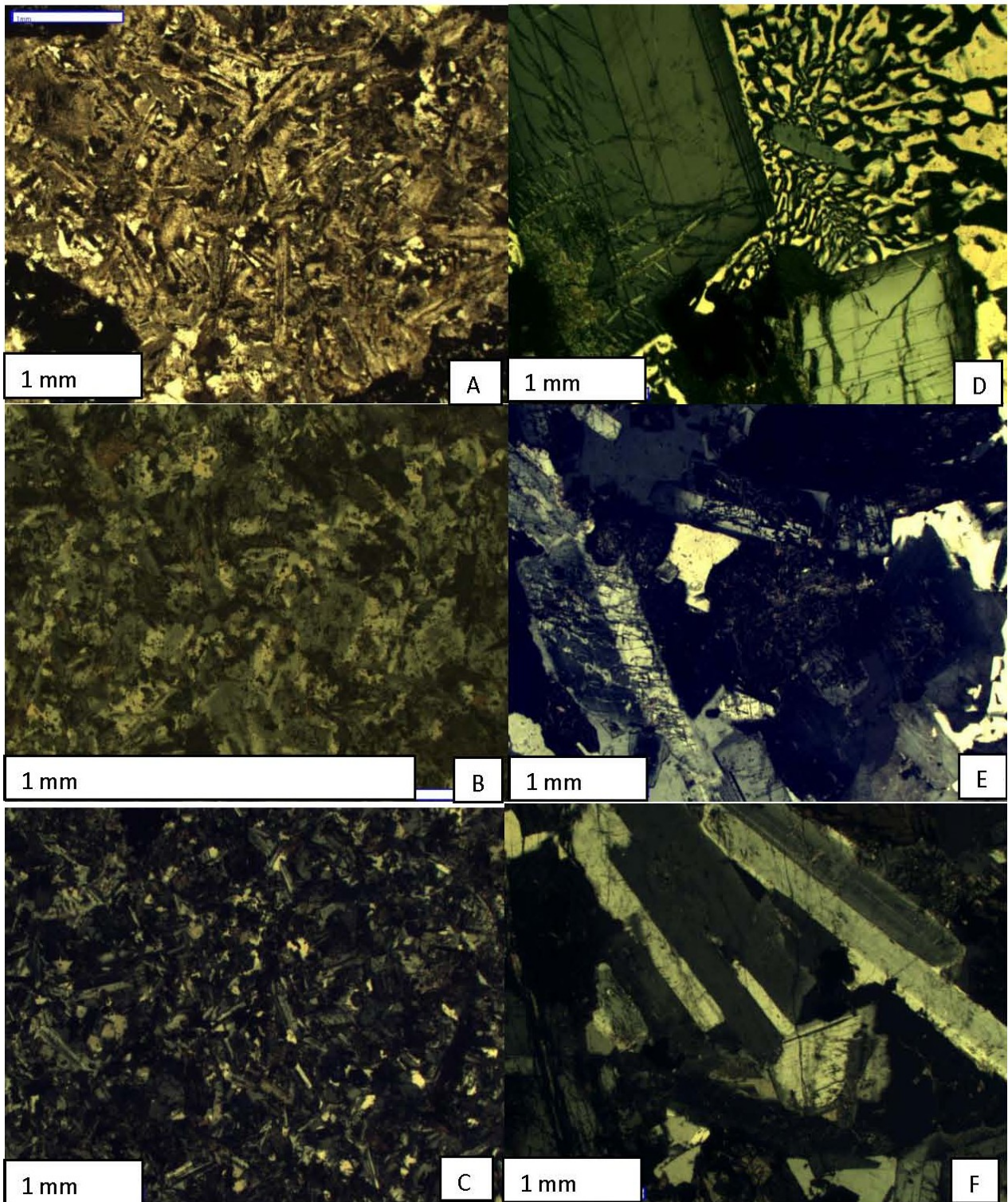


Figure 9: Comparison of igneous textures of breccia matrix (A,B,C) with end-of-hole igneous rock (D,E,F). Note similar crystal arrangement across all photomicrographs, but the texture preserved in the breccia matrix is finer grained. A) L02-02-94 B) L02-02-183 C) L02-02-191 D) L02-02-231 E) L02-02-240 F) L02-02-257.

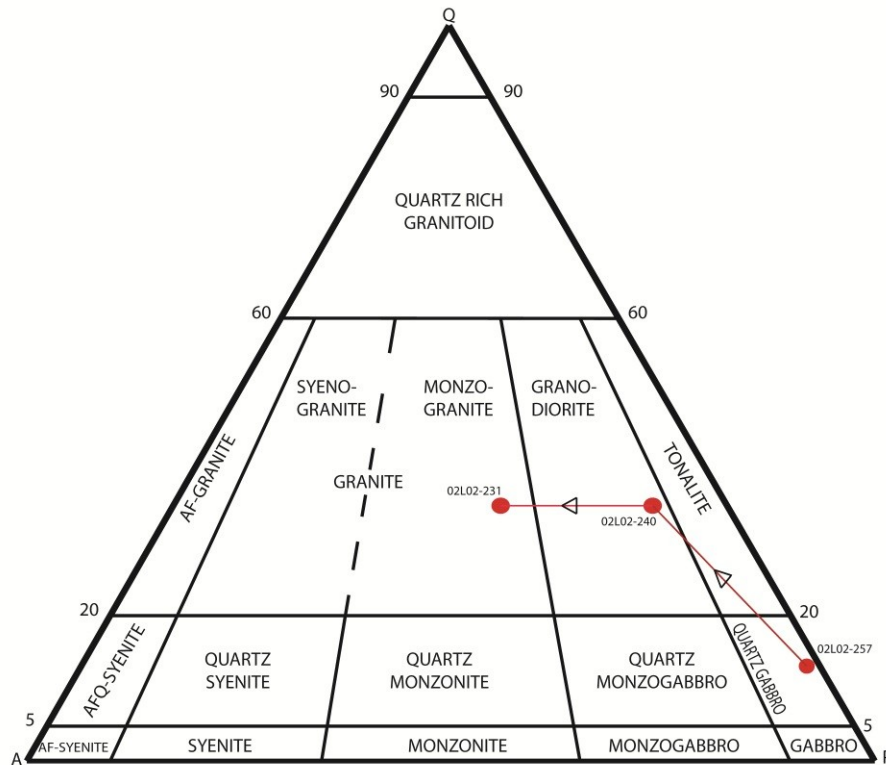


Figure 10: Schematic QAP diagram demonstrating end-of-hole rock lithology based on normalized point counts. Note increasing modal percentage of felsic mineralogies up-section.

SEM Analysis

Since petrographic techniques were adequate for identifying the end-of-hole igneous rock mineralogy, SEM-EDS analysis focused on the fine-grained breccia matrix. Data tables and images representing EDS spot analysis derived weight percent of elements are provided in Appendix D. The matrix is relatively rich in felsic minerals, with most of the “mafic” elements coalesced into the phases of amphibole, clinopyroxene or chlorite, each of which occurs in moderate to low abundance. It should be noted that this method is semi-quantitative, so elemental abundances derived and mineral phases derived from them are subject to a relatively large margin of error (~20%). This method is not sensitive enough to

quantify trace elements (e.g. Cr, Zn, Ti, Br, etc), so data representing these elements is not reliable. Figure 12 synthesises both petrographically delineated mineralogy and SEM derived mineral phases to deduce hypothetical mineral reactions, and Figure 11 qualitatively represents relative abundances of mineral phases in matrix based on SEM-EDS analysis.

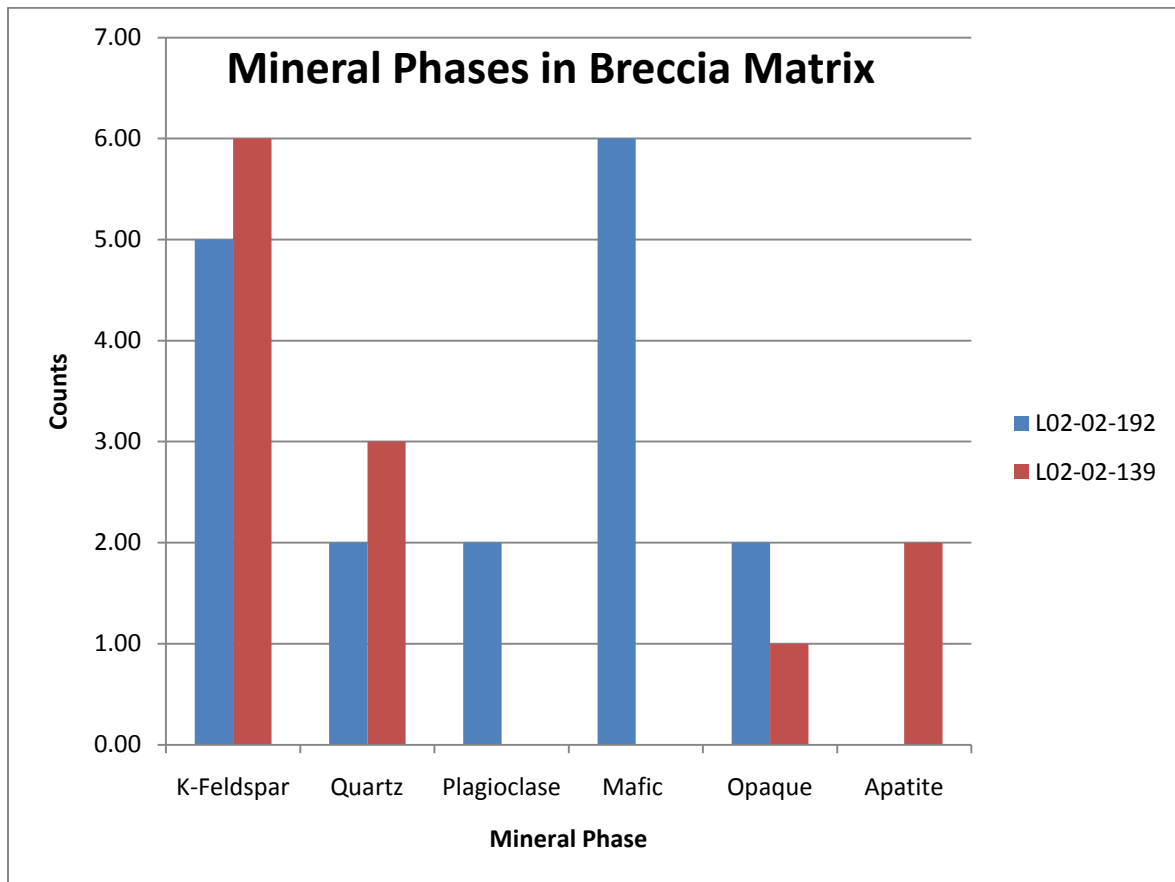


Figure 11: Relative abundances of minerals in breccia matrix based on SEM-EDS elemental determination. Sites of interest representing the breccia matrix as whole were used from samples L02-02-192 and L02-02-139. Spectra were attributed mineral phases based on relative weight percent of elements, and then counted and presented above. Mafic minerals include amphibole, chlorite, and clinopyroxene. All analyzed sites are further defined in Appendix D.

Discussion

Cause of Brecciation

Two general mechanisms are hypothesized for breccia formation: (1) a primary mantle derived phase, predating intrusion of the Tamarack and (2) a secondary phase contemporaneous with or postdating intrusion of the Tamarack. Evidence for the first would be dominant mafic mineral assemblages in the breccia matrix and the presence of mantle chemical signatures. Evidence for the second would be a breccia matrix broadly comparable to the granophyre gabbro norite sidewall of the Tamarack Intrusion. SEM-EDS and petrographic observations indicate that the breccia matrix is more felsic than the Tamarack body and comparable to the end-of-hole igneous rocks, specifically the monzogranite (Figure 10). Preservation of end-of-hole igneous texture in the breccia matrix (Figure 9 D,E,F) supports this conclusion, as it provides a direct visual connection to the source rock. The end-of-hole igneous rock is hypothesized to have formed from the melting of Thomson Formation metasediments.

Given that the grain size of end-of-hole igneous rock increases up-section (Figure 9), it is likely continued melting and crystallization of Thomson Formation metasediments took place after breccia pipe formation. This indicates brecciation occurred early in the intrusion-melting processes, as more time was necessary in order to allow crystal growth to the larger observed size. In conjunction, these data imply the breccia is contemporaneous with or postdates intrusion of the upper lherzolite in the body of the Tamarack. The sphericity, concentric foliations and overall alteration of shape of the graphitic clasts indicates a high energy, if not explosive brecciation process, commonly attributed to felsic material with high volatile content. In this case, the metasediments are

assumed to be hydrous since (1) they are partly composed of hydrous minerals and (2) they possess meteoric groundwater in fractures. With the addition of heat phreatomagmatic explosive brecciation may occur. Water may have also been provided as the main body of the Tamarack Intrusion cooled, and metasomatism allowed water to flow through the surrounding area including through fractures and the breccia pipe. This water, in addition to meteoric water, may have caused the severe alteration of the matrix as observed today.

Hypothetical Mineral Reactions

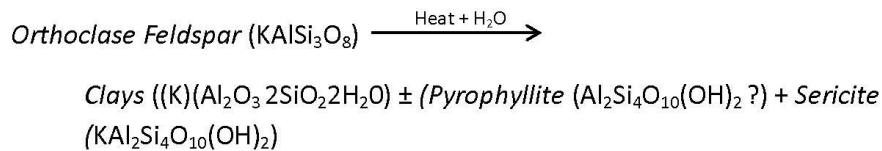
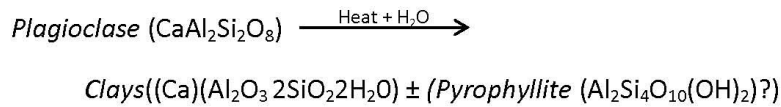
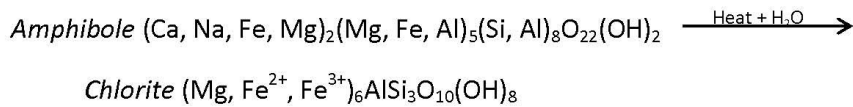
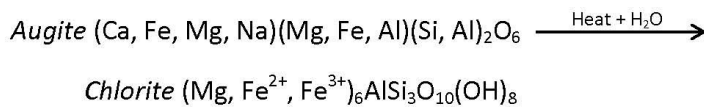
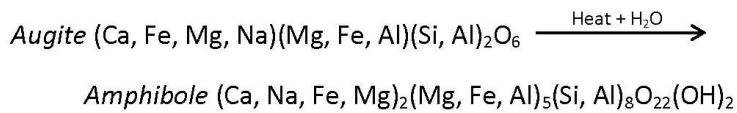
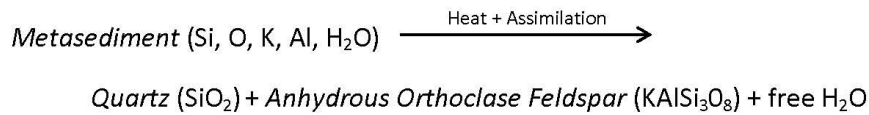


Figure 12: Proposed schematic mineral reactions from petrography and SEM observations.

Formation Model

Breccia pipe formation remains an unresolved and continually debated phenomenon. An objective classification scheme remains elusive, but textures and mineralogy can lead to understanding of formation processes (Sillitoe, 1985). In the case of the observed breccia pipe two general models are possible.

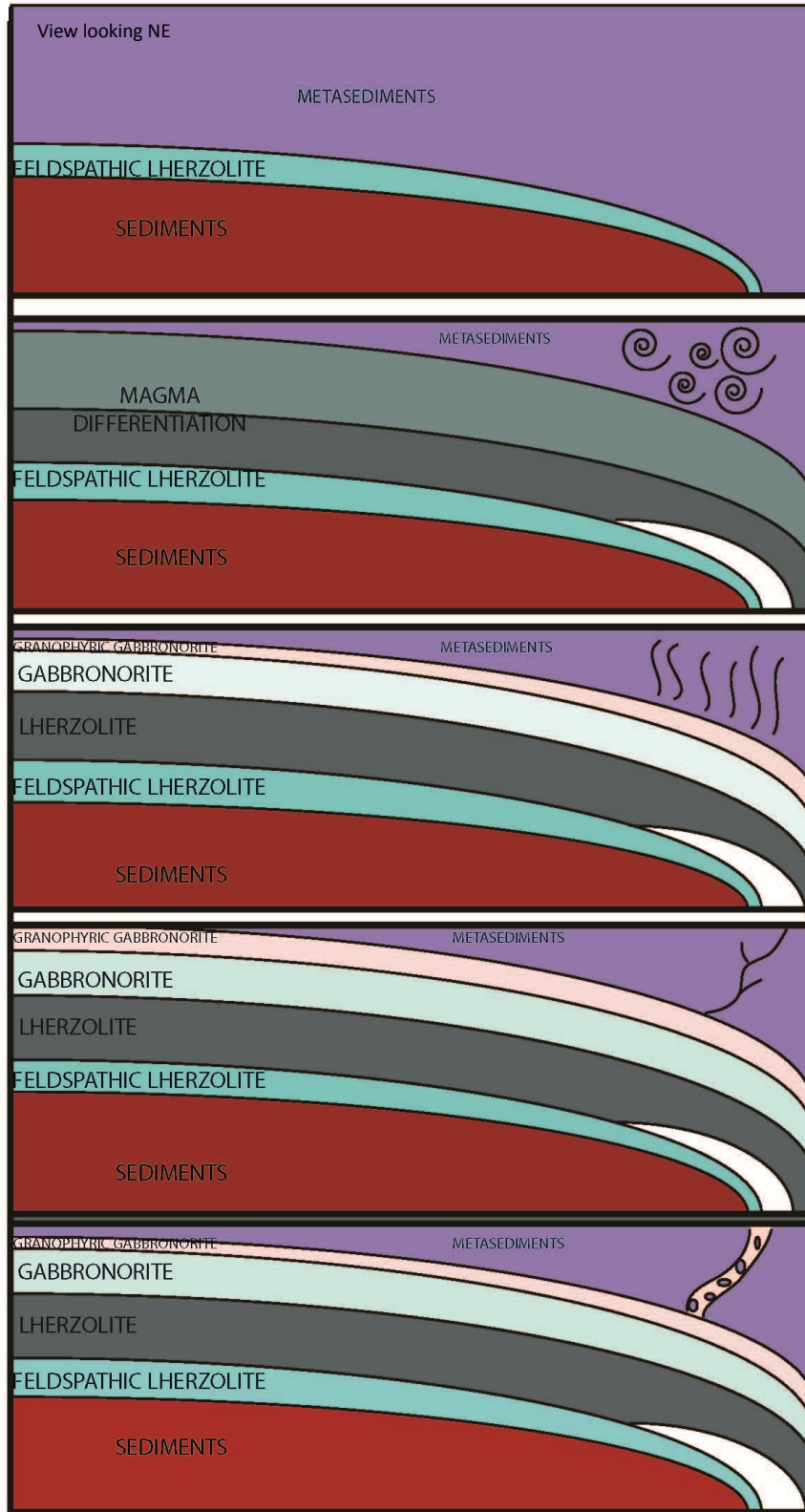
One possibility is a relatively quiescent emplacement of the breccia pipe. This would be characteristic of a Newtonian mafic magma, with a low volatile content. Brecciation would occur before emplacement of the intrusion, with parent magma rising into and through heterogeneities or fractures in the metasediments due to density difference between the two. As the intrusion rises, velocity and heat of the magma increases, causing the incorporation and transportation of country rock fragments, in this case carbon rich clasts. Brecciation terminates once the intrusion cools, or overtakes the breccia in cross-section. Being that the breccia matrix is not mafic, this model is not advocated.

The alternative model (Figure 13) assumes magma intrusion caused melting of the country rock, in this case the low grade metasediments of the Thomson Formation. These metasediments contained water in fractures and hydrous mineral phases, and fluid flow began after initial heating which caused or amplified weaknesses in the country rock. Once the energy of the melted sediment exceeded the cohesive strength of the weakened country rock an explosive event forced the adjacent magma through previously developed planes of weakness and concurrently developed fractures, causing incorporation of country rock fragments and breccia pipe formation. A generalized cross section of the post-tectonic relationship between the breccia pipe and Tamarack Intrusion is provided (Figure 15). The

explosive nature of the formation is reasonable since the melted country rock is relatively enriched in quartz and feldspar, thus likely volatile. In addition, being the molten rock type adjacent to the metasediments, the end-of-hole igneous rock (melted metasediment) is the most likely to fill the void. This is evidenced by breccia matrix mineralogy similar to the end-of-hole igneous rock. The presence of metasomatic minerals and graphic texture also supports this fluid rich-model.

B

B'



See Figure 14 below for Geographic setting

INITIAL HEATING

DRIVING OFF OF WATER

DEVELOPMENT OF FRACTURES IN METASEDIMENT

EXPLOSIVE BRECCIA PIPE FORMATION

Figure 13: Proposed schematic process of breccia pipe formation, view looking NE. Modified from Goldner (2011).

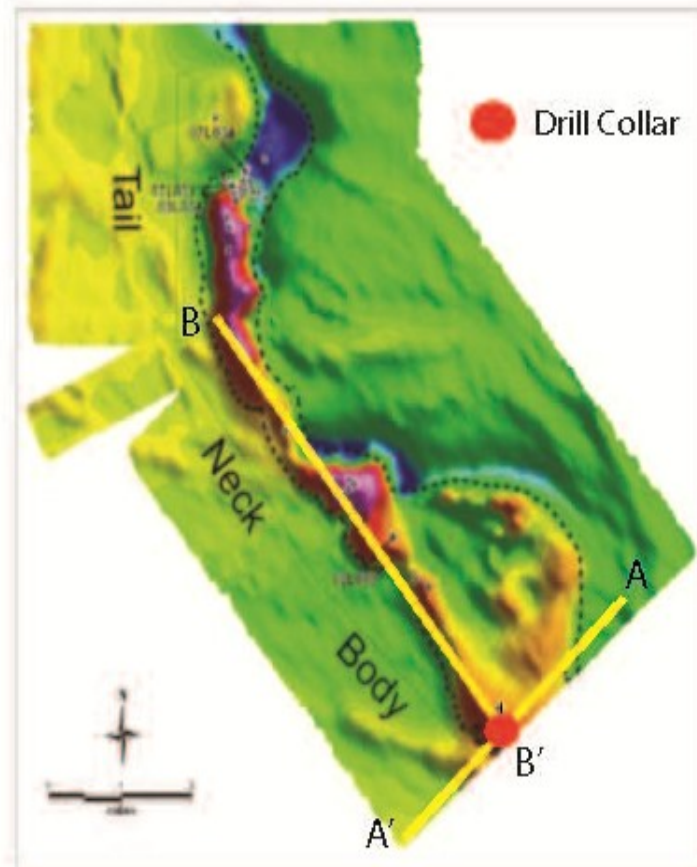


Figure 14: Map view depicting hypothetical cross section lines used in Figure 13 and Figure 15. Modified from Goldner (2011).

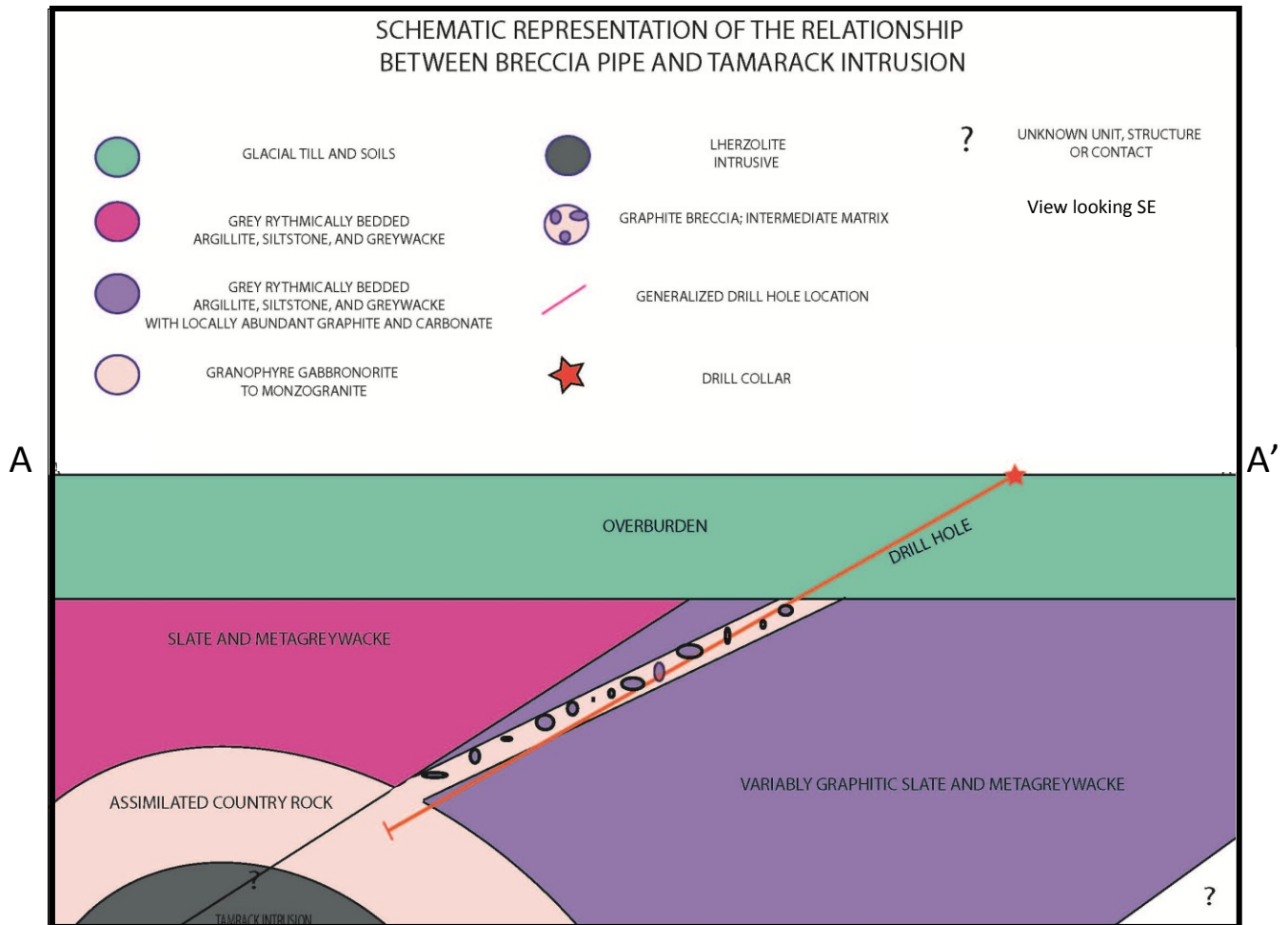


Figure 15: Hypothetical cross section of breccia pipe in relation to the Tamarack Intrusion. Modified from Boerboom (2009).

Conclusion

Petrographic and compositional data support the hypothesis that the breccia pipe represents a secondary phase synchronous with or post-dating intrusion of the Tamarack Intrusion. SEM-EDS analysis of the breccia matrix, when qualitatively combined and compared with alteration mineral assemblages delineated by petrographic analysis, indicate a relative abundance of felsic mineralogies. Petrographic analysis yields a quartz gabbro, granodiorite, and monzogranite respectively up-section, which represent the end-

of-hole igneous rock (melted country rock) adjacent to the breccia (Figure 15). The greatest proportion of felsic material occurs closest to the breccia. End-of-hole igneous rocks are then correlative to the breccia matrix, indicating the igneous rocks formed during intrusion and melting of metasediments are the source for the breccia pipe. Given the inherently high levels of volatiles, they also likely served as a major contributor to the formation of the breccia. The intense alteration of the matrix is the result of metasomatism, metamorphic fluids and circulation of meteoric groundwater during and after intrusion of the Tamarack.

Additional bulk sampling of the matrix for x-ray diffraction study would aid considerably in solidifying the above conclusions. Most importantly, additional drilling is necessary to develop a three-dimensional perspective and a direct contact between the base of the breccia and adjacent lithology. This contact is the most relevant spatial component, as it would objectively define the source of the breccia.

References Cited

- Boerboom, T.J. 2009. County atlas series atlas C-19, PART A Plate 2—Bedrock Geology. Minnesota Geological Survey, 1 p. (map)
- Boerboom, T.J. 2009. County atlas series atlas C-19, PART A Plate 6—Bedrock Geology. Minnesota Geological Survey, 1 p. (map)
- Chandler, V. W., Boerboom, T.J., Jirsa, M.A. 2007. Penokean tectonics along a promontory-embayment margin in east-central Minnesota. *Precambrian Research*, 157, 26-49.
- Goldner, B.D. 2011. Petrology of the Ni-Cu-PGE mineralized Tamarack Intrusion, Aitkin and Carlton Counties, Minnesota. Masters Thesis, University of Minnesota, 1-151.
- Holm, D. K., Schneider, D. A., Rose, S., Mancuso, C., McKenzie, M., Foland, K. A., Hodges, K. V. 2007. Proterozoic metamorphism and cooling in the southern Lake Superior region, North America and its bearing on crustal evolution. *Precambrian Research*, 157, 106-126.
- Holm, D. K., Anderson, R., Boerboom, T. J., Cannon, William F., Chandler, Val W., Jirsa, M. A., Miller, J., Schneider, D. A., Schulz, Klaus J., Van Schmus, W. R. 2007. Reinterpretation of Paleoproterozoic accretionary boundaries of the north-central United States based on a new aeromagnetic-geologic compilation. *Precambrian Research*, 157, 71-79.
- Hronsky, J.M.A. 2011. Self ordered critical systems and ore formation: The key to spatial targeting? SEG Newsletter, 84.
- Hutchinson, C. H. 1983. Economic deposits and their tectonic setting. John Wiley and Sons, Inc., New York, 104.
- Le Maitre, R. W. (ed.) 2002. Igneous Rocks. A Classification and Glossary of Terms. Recommendations of the International Union of Geological Sciences Subcommittee on the Systematics of Igneous Rocks, 2nd ed.
- Mccallum, M. E. 1985. Experimental evidence for fluidization processes in breccia pipe formation. *Economic Geology and the Bulletin of the Society of Economic Geologists*, 80, 1523-1543.
- Piercey, P., Schneider, D. A., Holm, Daniel K. 2007. Geochronology of Proterozoic metamorphism in the deformed Southern Province, northern Lake Huron region, Canada. *Precambrian Research*, 157, 127-143.
- Schulz, K. J., Cannon, William F. 2007. The Penokean Orogeny in the Lake Superior region. *Precambrian Research*, 157, 4-25.

- Sillitoe, R. H. 1985. Ore-related breccias in volcanoplutonic arcs. *Economic Geology and the Bulletin of the Society of Economic Geologists*, 80, 1467-1514.
- Tohver, E., Holm, D.K., Van der Pluijm, B.A., Essene, E.J., Cambray, F.W. 2007. Late Paleoproterozoic (geon 18 and 17) reactivation of the Neoproterozoic Great Lakes tectonic zone, northern Michigan, USA; evidence from kinematic analysis, thermobarometry and (super 40) Ar/ (super 39) Ar geochronology. *Precambrian Research*, 157, 144-168.
- Van Schmus, W. R., Schneider, D. A., Holm, Daniel K., Dodson, S., Nelson, B. K. 2007. New insights into the southern margin of the Archean-Proterozoic boundary in the north-central United States based on U/Pb, Sm/Nd, and Ar/Ar geochronology. *Precambrian Research*, 157, 80-105.
- Vervoort, J. D., Wirth, K., Kennedy, B., Sandland, T., Harpp, K.S. 2007. The magmatic evolution of the Midcontinent Rift; new geochronologic and geochemical evidence from felsic magmatism. *Precambrian Research*, 157, 235-268.
- Wolfe, J. A. 1980. Fluidization versus phreatomagmatic explosions in breccia pipes. *Economic Geology and the Bulletin of the Society of Economic Geologists*, 75, 1105-1109.

Appendix

- A) Informal Core Log
- B) Core Descriptions
- C) Petrographic Data
- D) SEM Data

Appendix A.) Informal-Field Core Log

Core Logging Hole #02-L02

Logged June 2, 2010

Michael Hendrickson Kennecott Exploration (Rio Tinto)

Sunday July 25, 2010

Consistent Brecciation Begins at 66.75 meters (intense alteration ceases)

Depth (meters)	Description
66.75-67	angular graphitic inclusions(1mm-3cm); elongate rounded graphitic inclusions dominate (highest% composition); 1mm-1cm in diameter clasts set in fine grained matrix (pyroxene?/plagioclase?) 25-35% graphite composition minor sulfide presence
67-67.5	Dominant graphitic presence (no brecciation) sulfides present in greater amount (arsenopyrite/pyrrhotite)
67.5-67.6	angular graphitic inclusions (1mm-3cm); elongate rounded graphitic inclusions dominate (highest% composition); 1mm-1cm in diameter clasts set in fine grained matrix (pyroxene?/plagioclase?) 25-35% graphite composition minor sulfide presence
67.6-67.67	Dominant graphitic presence (no brecciation) sulfides present in greater amount (arsenopyrite/pyrrhotite)
67.67-72.20	Continuation of features seen in [66.67-67] 30% graphite composition some zones dominated entirely of graphite are seen in this section presence of angular clasts increases downcore in this section fine grained matrix
72.20-74.95	Coarser grained matrix - darker color graphitic inclusion size large(~73mm) % composition varies from 20-40% at ~72.4 dendritic/ finger like crystals of plagioclase present *sample taken

74.95-77.82	<p>even coarser grained matrix</p> <p>same clast character as before</p> <p>some angular</p> <p>most rounded</p> <p>constitently larger (5mm-3cm)</p> <p>some minor sulfide present</p> <p>this continues to <u>86.48 meters</u></p>
86.48-92.07	<p>character remains similar</p> <p>clast size becomes more equigranular and smaller (1mm-1.5cm)</p>
92.07-94.92	<p>character remains same</p> <p>clast size becomes smaller on average (1mm-5mm)</p> <p>mica present</p>
94.92-97.83	<p>clast size increases around 96.5 m</p> <p>% composition increases to > 40%</p> <p>matrix grain size increases</p> <p>fingering crystals of plagioclase present</p>
97.83-100.61	<p>Trend continues through ~98.3m</p> <p>at which point % composition decreases to ~25-35%</p> <p>clasts become smaller, and more homogeneous in size</p> <p>larger matrix grain size</p> <p>minor sulfide present</p> <p>same trend continues <u>through ~103m</u></p>
103.3-106.58	<p>matrix grain size same as above</p> <p>Larger/fewer more angular clasts present</p> <p>presence of mica (disseminated)</p>
106.58-109.92	<p>107-108</p> <p>grades back to smaller and more abundant graphite clasts</p> <p>more rounded</p> <p>108-108.5</p> <p>high content disseminated graphite >50%</p> <p>108.5- 109.42</p> <p>angular, elongate, and rounded clasts present</p> <p>(2mm-3cm) ~30% composition</p>

109.42-112.16	109.42-111 dominant graphite (massive phase ~100% composition) 111-112.16 30% composition-rounded (2mm-2cm diameter)
112.16-114.8	continuation of last description towards greater depth grades to 10-15% graphite composition clasts rounded (2mm-2cm diameter)
114.8-116	continues gradation to 5% composition finer grained matrix appears
116-118.7	~1% graphite composition small rounded and angular crystals. eventually grades to near 0% graphite composition
118.7-121.62	near 0% composition finer matrix 121.62-123.16 grades back up to 10% composition small clasts (1mm-1cm)
123.16-126	gradual gradation back to larger clast size and % composition (5cm, ~30% respectively) quartz veining present
126-128.7	less abrupt continuation of last gradation phase
128.7-131.4	gradation into lighter color (finer matrix) appearance of larger crystals and, but %comp still floating at ~30%
131.4-134.25	continuation of trend ~40% comp towards lowering depth quartz veining present @ 132m "chill margins" or "halos" form around inclusions (lighter color than matrix)

134.25-137.6	Halos continue through ~136.5M halos change color at 134.25 to rusty color then change back at ~135m quartz veining at 134.75m % composition drops at ~137m to ~10-15%
137.6-140	Rings appear again, not as well defined %comp increases to 20-30% same character of clast size and distribution seen in previously adjacent section of core metasediments hit @ 139.5 (folded sediments, source of breccia producing liquid?)
140-142.75	140-140.5 intrusion (same as above) cuts sediments metasediments found throughout rest of section with pockets of partial melt
142.75-145.55	sediment with minor quartz clasts layering can be turbiditic (thomson formation) well defined folding pockets of partial melt (interstitial pockets of pink mineral, k-feldspar most likely) sediment continues through 182.75
182.75-185.62	breccia appears again same character as seen right before sediments
185.62-187.54	same sediments
187.54-190.33	breccia begins again k-feldspar, sulfide, and quartz pockets present rim around graphite inclusions present starts at ~20% comp and grades to 35% comp at 196m
196-198.78	same metasediments
198.78-201.56	same sediments quartz veining interstitial melt pockets (k-feldspar)

217-221.2	<p>breccia begins again</p> <p>finer grained matrix</p> <p>more angular clasts possessing planar fabric</p> <p>some sulfide (pyrrhotite, arsenopyrite)</p> <p>~30-40% clast composition</p> <p>hematite rings just inside clasts starts at</p> <p>~219-221.5</p>
221.2-223.35	<p>coarser grained matrix</p> <p>elongate ~1-4cm graphitic inclusions</p> <p>perpendicular to core wall</p> <p>%composition drops to ~20%, this continues through</p> <p>223 igneous starts, the description in core log deems this syenite</p> <p>more than likely it is not syenite, but something more plagioclase rich, quartz monzonite?</p>
223.35-226.85	<p>same quartz monzonite?</p> <p>plag/ kfeldspar. 50/50?</p> <p>grades into increasing presence of k-feldspar</p> <p>within a few fractions of a meter grades back into less k-feldspar</p> <p>medium grain size</p> <p>continues to <u>241.2m</u></p>
241.2-255.73	<p>Igneous rock</p> <p>plagioclase rich with (mafic minerals?)</p>

Appendix B.)Core Descriptions

L02-02-67-Breccia

This portion of core is light green to black, graphite dominated. This specimen contains the following minerals: 5% yellow to silver anhedral pyrite 1mm-5mm diameter clustered in graphite clasts; 25% black poikiloblastic graphite clasts that are subhedral ranging in diameter from 1mm-4mm; 70% intermediate to felsic matrix that is light tan to green color.

See Appendix D for SEM-EDS derived wt% of elements in matrix.

L02-02-69-Breccia

This portion of core is light green to black, graphite dominated, with an intermediate to felsic matrix. This sample contains the following minerals: <5% yellow pyrite as .5-1mm pyritihedrons or cubes; 10% yellow to orange alteration mineral (epidote?) surrounding graphite clasts; 40% anhedral and skeletal black graphite clasts 1mm-10m diameter; 40% light green intermediate to felsic matrix, that contains black euhedral laths 1-2mm long and .25-.5mm wide; The matrix appears to be highly altered.

See Appendix D for SEM-EDS derived wt% of elements in matrix.

L02-02-79-Breccia

This specimen is green to black with black graphite clasts. This specimen contains the following minerals: 60% black anhedral and poikiloblastic graphite clasts .5mm-20mm in diameter; 40% light green to dark green matrix of felsic to intermediate composition.

See Appendix D for SEM-EDS derived wt% of elements in matrix.

L02-02-85-Breccia

This portion of core is black to green with graphite clasts. This specimen contains the following minerals: <1% anhedral hematite masses, 1mm in diameter within graphite clasts; 50% green matrix of felsic to intermediate mineralogy; 50% black, 1mm-20mm diameter anhedral-round graphite clasts. Specimen is altered.

See Appendix D for SEM-EDS derived wt% of elements in matrix.

L02-02-94-Breccia

This portion of core is green to black, and possesses graphite clasts. This specimen contains the following minerals: <1% yellow pyrite as <1mm anhedral masses in graphite clasts; 70% brown to green matrix of felsic to intermediate mineralogy with <1mm x .1mm white euhedral laths of unknown mineralogy; 20% anhedral and black 3mm-10mm in diameter graphite clasts.

See Appendix D for SEM-EDS derived wt% of elements in matrix.

L02-02-101-Breccia

This portion of core is black to green, black graphite dominated, with matrix mineralogy ranging from intermediate to felsic. This sample contains the following minerals: 80% black graphite subhedral to anhedral poikiloblastic clasts 1mm-10mm in diameter; 5% yellow to silver pyrite or arsenopyrite as 1 mm cubic or pyritihedron or anhedral masses 3-

6mm in diameter; 15% light green intermediate to felsic matrix with white euhedral laths 1-2mm long and .25-.5 mm wide. The matrix is altered.

See Appendix D for SEM-EDS derived wt% of elements in matrix.

L02-02-115-Breccia

This portion of core is green to dark green, possesses graphite clasts, and is matrix dominated. This sample contains the following minerals: <5% yellow pyrite as anhedral masses in matrix, 1-2mm in diameter; 15% black anhedral and poikiloblastic graphite inclusions 1mm-15mm in diameter; 40% green to dark green matrix of alkali to intermediate mineralogy. Minor alteration is also present.

See Appendix D for SEM-EDS derived wt% of elements in matrix.

L02-02-133-Breccia

This specimen is light green to green and possesses graphite clasts. The specimen contains the following minerals: 15% .5-2cm diameter anhedral to acicular poikiloblastic black graphite clasts; <1% yellow, anhedral, and 1mm diameter pyrite within graphite clasts; 90% light green to green matrix of intermediate to felsic mineralogy and crystal geometry. A light green halo surrounds graphite clasts.

See Appendix D for SEM-EDS derived wt% of elements in matrix.

L02-02-139-Breccia

This portion of core is dark green to black with black graphite clasts. This specimen contains the following minerals: 90% dark green matrix of intermediate to felsic

mineralogy; 10% 1mm-10 mm in diameter subhedral graphite clasts; <1% yellow pyrite as anhedral masses within graphite clasts.

See Appendix D for SEM-EDS derived wt% of elements in matrix.

L02-02-179-Metasediment

This specimen is a black metasediment. This specimen contains the following minerals: 99% black siliceous metasediment; <1% acicular to subhedral 10mm x 1mm interstitial pockets of K-feldspar.

L02-02-183-Breccia

This portion of core is black to green containing black graphite clasts. This specimen contains the following minerals: <1% yellow pyrite in disseminated 1mm anhedral masses within graphite inclusions; 5% ~1mm red anhedral amoeboid interstitial pockets of K-feldspar; 30% black graphite anhedral to acicular clasts 1-3mm in diameter; 60% green matrix of intermediate to felsic mineralogy.

See Appendix D for SEM-EDS derived wt% of elements in matrix.

L02-02-191- Breccia

This portion of core is black, possessing black graphitic clasts. This specimen contains the following minerals: <5% yellow pyrite as anhedral masses, 1mm-10mm in diameter, and commonly adjacent to or within graphite clasts; 70% intermediate to felsic matrix; 30% subhedral and poikiloblastic 1mm-15mm diameter graphite clasts commonly haloed by unknown mineral; <5% red K-feldspar as anhedral interstitial masses 1-2mm in diameter.

See Appendix D for SEM-EDS derived wt% of elements in matrix.

L02-02-192-Breccia

This specimen is black to green possessing graphitic clasts. This specimen contains the following minerals: 50% felsic to intermediate matrix; 50% .5-1.5 cm black poikiloblastic graphite clasts that are anhedral and surrounded by light green halos of unknown mineralogy; < 5% <1mm anhedral pockets of K-feldspar hosted in metasediments; <1% anhedral masses of yellow pyrite ranging in size from 1-5mm in diameter; < 5% 1mm x .1mm acicular to subhedral yellow/orange mineral commonly found in graphite clasts, and rarely found in matrix.

See Appendix D for SEM-EDS derived wt% of elements in matrix.

L02-02-210-Metasediment

This specimen is a black metasedimentary rock with quartz veins. This specimen contains the following minerals: 90% black siliceous metasediment; 10% laterally continuous and parallel segments of red K-feldspar ~3cm long and ~.3cm wide located in bottom right half of sample; <5% quartz as 3cm long and .2cm wide veins spanning top to bottom of sample. There is variably spaced and irregular fracturing present trending EW across specimen.

L02-02-221-Breccia

This portion of core is dark green with graphite clasts. This specimen contains the following minerals: <1% yellow anhedral pyrite 1mm in diameter within graphite clasts; 90% felsic to intermediate dark green matrix with <1mm x .1mm acicular white to yellow

laths of unknown mineralogy; 15% 1-3mm anhedral to acicular graphite clasts with hematite halos.

See Appendix D for SEM-EDS derived wt% of elements in matrix.

L02-02-222-Breccia

This portion of core is green to dark green to yellow, possesses graphite inclusions, and is matrix dominated. This sample contains the following minerals: <5% yellow pyrite as ~1mm anhedral masses commonly adjacent to graphite or in graphite clasts; 20% black anhedral graphite clasts ranging in diameter from 1mm-10 mm; <1% pink K-feldspar as <1mm diameter anhedral masses; 90% green to dark green matrix with yellow minerals, that is intermediate to felsic composition.

See Appendix D for SEM-EDS derived wt% of elements in matrix.

L02-02-228-Chloritized Monzogranite

This portion of core is a black to red chloritized monzogranite. See Appendix C for modal percentages of minerals.

Nearly no primary plagioclase remaining, 1mm-6mm x 1mm-6mm interstitial anhedral quartz. 2mm-6mm x 3mm-7mm graphic to granophyre textures of K-feldspar and quartz. .25mm-.5mm x 5mm-8mm acicular apatite, .25mm x .25 mm in cross section. .5mm-1mm x .5mm-1mm euhedral to anhedral that are occasionally skeletal opaques. 1mm-5mm x 1mm-10mm chlorite masses that are anhedral/ sub-hedral and interbolate.

Alteration: Clay, Sericite, Pyrophyllite, Chlorite. Chlorite masses are euhedral to anhedral, .5mm-3mm x .5mm-5mm and interstitial to plagioclase laths. Clay, sericite, and pyrophyllite masses are euhedral to anhedral, 1mm-4mm x 1mm-5mm, replacing plagioclase or K-feldspar.

L02-02-231-Monzogranite

This specimen is a red to black monzogranite. See Appendix C for modal percentages of minerals.

2mm-8mm x 1mm-4mm euhedral, inequalgranular and holocrystalline plagioclase laths that are zoned and twinned. 2mm-6mm x 2mm-6mm graphic to granophyre textures of K-feldspar and quartz. 1mm-4mm x 1mm-3mm anhedral interstitial quartz with amoeboid boundaries.

Alteration: Clay, Sericite, Pyrophyllite, Chlorite. Chlorite masses are euhedral to anhedral, .5mm-1mm x .5mm-2mm and interstitial to plagioclase laths. Clay, sericite, and pyrophyllite masses are euhedral to anhedral, .5mm-1mm x .5mm-1mm, replacing plagioclase or K-feldspar.

L02-02-240-Granodiorite

This portion of core is grey to blue to red granodiorite. See Appendix C for modal percentages of minerals

.5mm-2mm x 1mm-6mm sub-hedral, zoned and twinned, interlocking, inequalgranular, holocrystalline plagioclase laths with polygonal grain boundaries. 1mm-2mm x 1mm-8mm anhedral quartz. 1mm-2mm x 1mm-2mm graphic/ granophyre texture of quartz and K-

spar. .5mm-1mm x .5mm-1mm euhedral to anhedral opaques. .5mm-1mm x .5mm-1mm euhedral to anhedral opaques.

Alteration: Clay, Chlorite, Sericite, Pyrophyllite. Chlorite masses are euhedral to anhedral, .5mm-1mm x .5mm-2mm and interstitial to plagioclase laths. Clay, sericite, and pyrophyllite masses are euhedral to anhedral, .5mm-.5mm x .5mm-.5mm, replacing plagioclase or K-feldspar.

L02-02-257-Quartz Gabbro

This portion of core is a dark green quartz gabbro. See Appendix C for modal percentages of minerals.

2mm-5mm x .5mm-1mm zoned and twinned, holocrystalline, inequalgranular, and interlocking plagioclase laths with polygonal grain boundaries. 1mm-3mm x 1mm-3mm amoeboid interstitial quartz and K-spar. 1mm-2mm x 1mm-2mm subhedral biotite. .5mm-1mm x .5mm-1mm anhedral opaques. 1mm-3mm x 1mm-2mm subhedral amphibole with distinct cleavage. .5mm-1mm x .5mm-1mm subhedral to anhedral augite crystals.

Alteration: Chlorite. Chlorite masses are euhedral to anhedral, .5mm-.5mm x .5mm-.5mm and interstitial to plagioclase laths.

Appendix C.) Petrographic Data

Modal percentages were delineated by point counting. Point counts varied from 700-2000 on a 27mm x 46mm thin section as a function of crystal size. Raw data was analyzed in Microsoft Excel in order to derive modal percentages of minerals. The majority of the modal percent attributed to pyrophyllite is clay or sericite. This is derived from qualitative SEM-EDS comparison to petrography; given SEM-EDS derived presence of potassium in matrix (Appendix D), and Si/Al ratios, a large percentage of clay and sericite is estimated.

02-L02-67		
	Points	Mode
Quartz	262	25.39%
Plagioclase	2	0.19%
Pyrophyllite	251	24.32%
Chlorite	210	20.35%
Brown alteration	2	0.19%
Ilmenite	8	0.78%
Unknown	0	0.00%
Carbon	297	28.78%
Total	1032	100.00%

02-L02-69		
	Points	Mode
Quartz	405	20.37%
Plagioclase	4	0.20%
Pyrophyllite	408	20.52%
Chlorite	320	16.10%
Brown alteration	108	5.43%
Ilmenite	59	2.97%
Unknown	0	0.00%
Carbon	684	34.41%
Total	1988	100.00%

02-L02-79		
	Points	Mode
Quartz	121	7.98%
Plagioclase	0	0.00%
Pyrophyllite	411	27.11%
Chlorite	171	11.28%
Brown alteration	106	6.99%
Opaque	3	0.20%
Carbon	704	46.44%
Total	1516	100.00%

02-L02-85		
	Points	Mode
Quartz	114	8.49%
Plagioclase	0	0.00%
Pyrophyllite	487	36.29%
Chlorite	207	15.42%
Brown alteration	0	0.00%
Opaque	1	0.07%
Carbon	507	37.78%
Hematite	26	1.94%
Total	1342	100.00%

02-L02-94		
	Points	Mode
Quartz	200	13.92%
Plagioclase	0	0.00%
Pyrophyllite	462	32.15%
Chlorite	80	5.57%
Brown alteration	199	13.85%
Opaque	13	0.90%
Carbon	483	33.61%
Total	1437	100.00%

02-L02-101		
	Points	Mode
Quartz	135	9.27%
Plagioclase	5	0.34%
Pyrophyllite	222	15.24%
Chlorite	335	22.99%
Brown alteration	48	3.29%
Opaque	10	0.69%
Carbon	702	48.18%
Total	1457	100.00%

02-L02-115		
	Points	Mode
Quartz	336	25.71%
Plagioclase	2	0.15%
Pyrophyllite	419	32.06%
Chlorite	264	20.20%
Brown alteration	53	4.06%
Opaque	6	0.46%
Carbon	227	17.37%
Total	1307	100.00%

02-L02-133		
	Points	Mode
Quartz	182	16.99%
Plagioclase	1	0.09%
Pyrophyllite	325	30.35%
Chlorite	224	20.92%
Brown alteration	115	10.74%
Opaque	24	2.24%
Carbon	159	14.85%
Amphibole	22	2.05%
Biotite	19	1.77%
Total	1071	100.00%

02-L02-139		
	Points	Mode
Quartz	194	15.93%
Plagioclase	0	0.00%
Pyrophyllite	320	26.27%
Chlorite	486	39.90%
Brown alteration	35	2.87%
Opaque	26	2.13%
Carbon	157	12.89%
Total	1218	100.00%

02-L02-183		
	Points	Mode
Quartz	67	6.95%
Plagioclase	340	35.27%
Pyrophyllite	161	16.70%
Chlorite	16	1.66%
Brown alteration	145	15.04%
Opaque	3	0.31%
Carbon	182	18.88%
Amphibole	34	3.53%
Biotite	16	1.66%
Total	964	100.00%

02-L02-191		
	Points	Mode
Quartz	71	7.20%
Plagioclase	341	34.58%
Pyrophyllite	184	18.66%
Chlorite	14	1.42%
Brown alteration	43	4.36%
Opaque	0	0.00%
Carbon	208	21.10%
Amphibole	25	2.54%
Augite	55	5.58%
Biotite	45	4.56%
Total	986	100.00%

02-L02-192		
	Points	Mode
Quartz	119	12.74%
Plagioclase	188	20.13%
Pyrophyllite	242	25.91%
Chlorite	5	0.54%
Brown alteration	162	17.34%
Opaque	14	1.50%
Carbon	174	18.63%
Amphibole	2	0.21%
Augite	15	1.61%
Biotite	13	1.39%
Total	934	100.00%

02-L02-221		
	Points	Mode
Quartz	121	11.69%
Plagioclase	5	0.48%
Pyrophyllite	329	31.79%
Chlorite	174	16.81%
Brown alteration	60	5.80%
Opaque	83	8.02%
Carbon	252	24.35%
Amphibole	1	0.10%
Augite	5	0.48%
Biotite	5	0.48%
Total	1035	100.00%

02-L02-222		
	Points	Mode
Quartz	149	13.98%
Plagioclase	3	0.28%
Pyrophyllite	280	26.27%
Chlorite	346	32.46%
Brown alteration	24	2.25%
Opaque	101	9.47%
Carbon	158	14.82%
Amphibole	0	0.00%
Augite	2	0.19%
Biotite	3	0.28%
Total	1066	100.00%

02-L02-228		
	Points	Mode
Quartz	226	19.47%
Plagioclase		0.00%
K-Feldspar	102	8.79%
biotite	64	5.51%
Chlorite	558	48.06%
Opaque	72	6.20%
Brown Alteration	112	9.65%
Apatite	27	2.33%
Total	1161	100.00%

02L02-231	Monzogranite	Points	Mode	Points	Normalized Mode
Plagioclase		222	32.99%	222	39.43%
Quartz		189	28.08%	189	33.57%
K-Feldspar		152	22.59%	152	27.00%
Biotite		17	2.53%		
Chlorite		50	7.43%		
Amphibole		25	3.71%		
Opaques		11	1.63%		
Alteration		7	1.04%		
Calcite		0	0		
Pyroxene		0	0		
Hematite		0	0		
Total		673	100.00%	563	100.00%

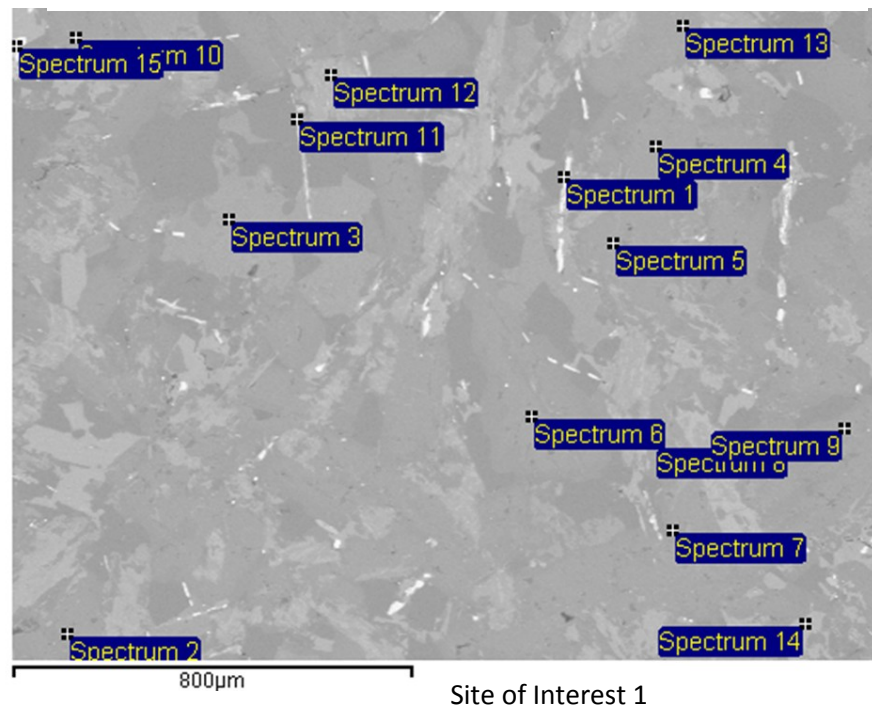
L02-02-240	Granodiorite	Points	Mode	Points	Normalized Mode
Plagioclase		564	38.11%	564	54.86%
Quartz		368	24.86%	368	35.80%
K-Feldspar		96	6.49%	96	9.34%
Biotite		91	6.15%		
Chlorite		85	5.74%		
Amphibole		2	0.14%		
Opaques		47	3.18%		
Alteration		227	15.34%		
Calcite		0			
Pyroxene		0			
Hematite		0			
Total		1480	100.00%	1028	100.00%

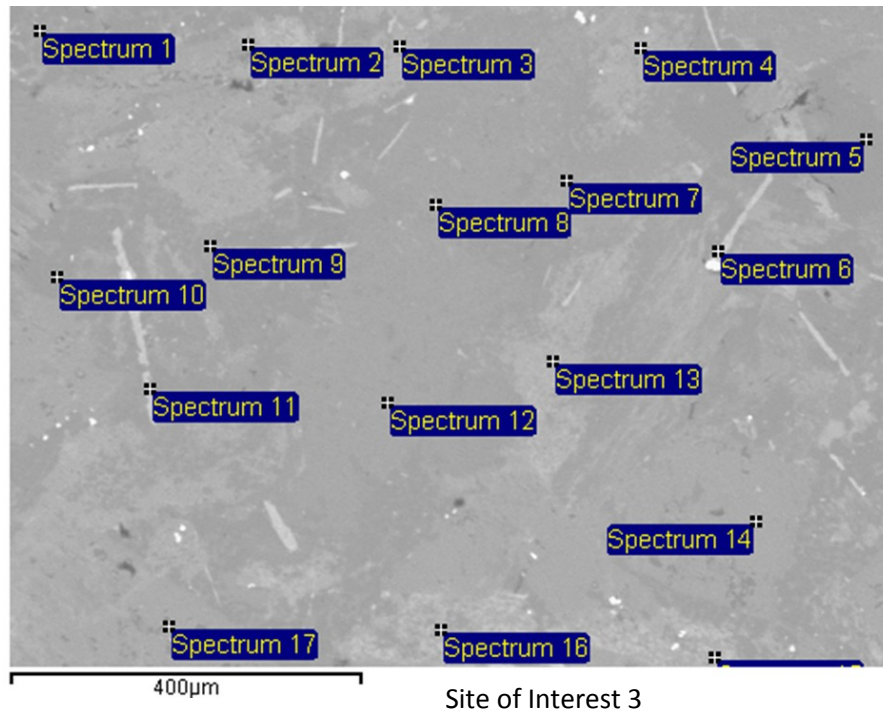
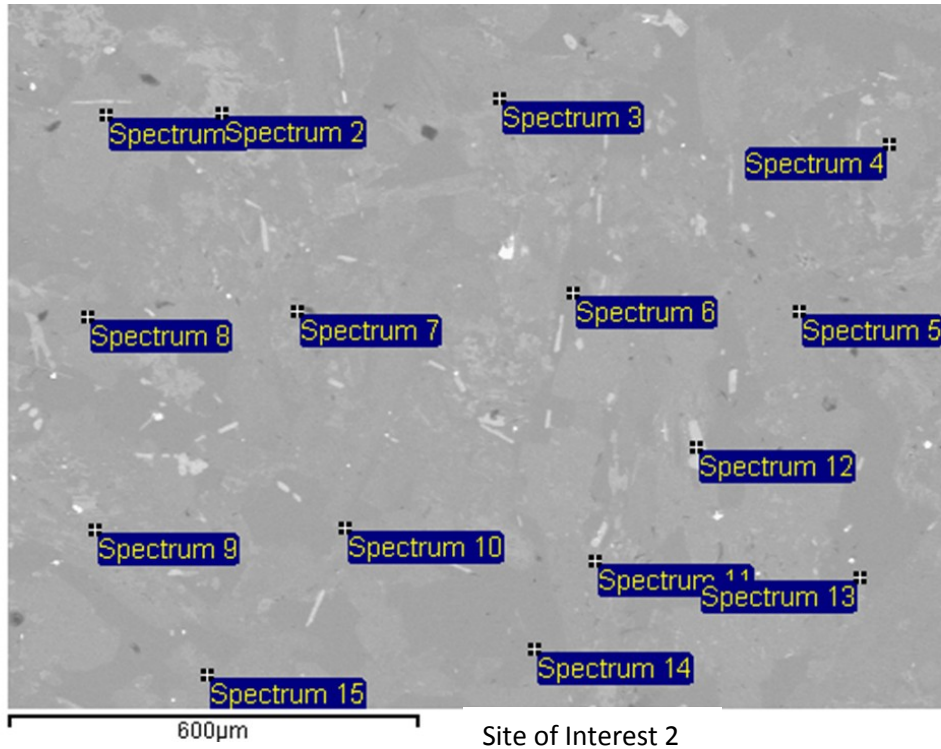
L02-02-257	Quartz Gabbro	Points	Mode	Points	Normalized Mode
Plagioclase		765	52.69%	765	86.15%
Quartz		114	7.85%	114	12.84%
K-Feldspar		9	0.62%	9	1.01%
Biotite		118	8.13%		
Chlorite		40	2.75%		
Amphibole		85	5.85%		
Opaques		206	14.19%		
Alteration		100	6.89%		
Calcite		6	0.41%		
Pyroxene		7	0.48%		
Hematite		2	0.14%		
Total		1452	100.00%	888	100.00%

Appendix D.) SEM DATA

All following data is presented in weight percent composition, and is only to be used qualitatively. All sites of interest are taken within the breccia matrix at specified depth given in the thin section ID; L02-02-***, last three digits signify depth in meters.

L02-02-192





columns are in element weight%

site of interest 1

ID: L02-02-192

	O	Na	Mg	Al	Si	K	Ca	Ti	Mn	Fe	Hypothesized Phase
Spectrum 1	41.36		3.66	3.79	9.33	5.00		10.51		20.45	Opaque
Spectrum 2	52.62	2.57		15.09	21.42		8.30				Plagioclase
Spectrum 3	50.41	1.20		8.37	22.90	17.11					K-Feldspar
Spectrum 4	53.23	2.43		14.39	21.05		8.89				Plagioclase
Spectrum 5	52.44	2.69		14.97	21.90		8.01				Plagioclase
Spectrum 6	52.20	2.58		15.10	21.79		8.33				Plagioclase
Spectrum 7	52.26	2.52		15.27	21.99		7.96				Plagioclase
Spectrum 8	54.75	4.48		11.09	23.41	2.24	0.86			3.17	K-Feldspar
Spectrum 9	51.39	2.02		15.55	21.17		8.70			1.17	Plagioclase
Spectrum 10	52.67	2.62		15.04	21.51		8.16				Plagioclase
Spectrum 11	49.31		5.97	6.64	13.89	5.19		2.42		16.57	Amphibole
Spectrum 12	57.89		2.83	1.87	3.62		25.85		1.00	6.93	Amphibole
Spectrum 13	51.85	2.43		15.55	21.44		8.74				Plagioclase
Spectrum 14	46.22		7.05	6.78	14.65	12.08		2.23		11.00	Opaque
Spectrum 15	47.56		6.47	6.53	14.03	11.84		2.25		11.32	Opaque

Site: Site of Interest 2

ID: L02-02-192

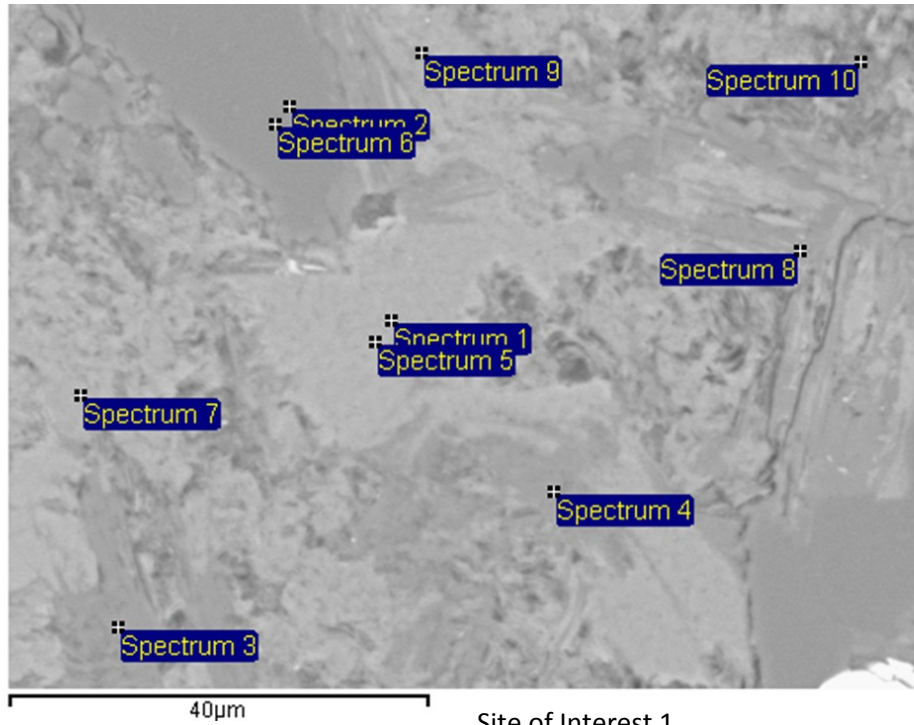
	O	Na	Mg	Al	Si	K	Ca	Ti	Mn	Fe	Hypothesized Phase
Spectrum 1	53.68			14.71	17.79		12.99			0.82	Plagioclase
Spectrum 2	55.35		5.04		19.42			0.49		19.70	Opaque
Spectrum 3	53.63	2.82		13.78	21.69		8.07				Plagioclase
Spectrum 4	53.64			14.37	18.09		13.23			0.67	Plagioclase
Spectrum 5	53.52			11.22	23.81		10.45			1.01	Plagioclase
Spectrum 6	58.61				41.39						Quartz
Spectrum 7	52.63	2.09	2.43	10.79	18.15		4.61			9.29	Amphibole?
Spectrum 8	55.39		1.34	14.63	18.00		8.50			2.13	Amphibole?
Spectrum 9	55.12	1.88		9.17	21.63		9.71	1.04		1.45	Amphibole?
Spectrum 10	54.14	5.23		11.13	25.33		3.66			0.51	Amphibole?
Spectrum 11	56.43		1.92	6.04	25.48		4.94		0.35	4.83	Amphibole?
Spectrum 12	45.48					17.39		37.13			K-Feldspar
Spectrum 13	58.47				41.53						Quartz
Spectrum 14	58.49				41.51						Quartz
Spectrum 15	53.90	2.01		13.99	20.26		9.33			0.51	Plagioclase

Site: Site of Interest 3

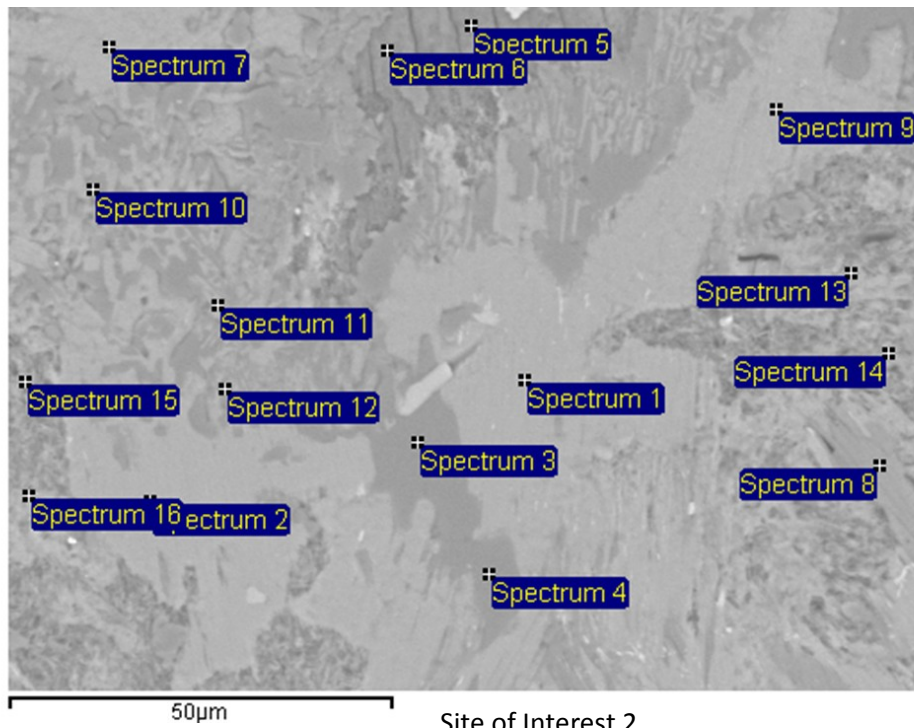
ID: L02-02-192

	O	Na	Mg	Al	Si	K	Ca	Ti	Mn	Fe	Hypothesized Phase
Spectrum 1	57.44	1.45		2.88	33.94	1.17		3.13			K-Feldspar
Spectrum 2	54.20	1.03		7.45	29.46	5.11	2.77				K-Feldspar
Spectrum 3	55.99		11.02		9.72		1.31		21.95		Mafic
Spectrum 4	53.33		11.26		5.71	1.13	1.27		20.04	7.26	Mafic
Spectrum 5	58.18				41.82						Quartz
Spectrum 6	51.05		1.04		5.83		3.91	35.46	2.72		Opaque
Spectrum 7	58.40		3.21		26.30		6.82		5.27		Mafic
Spectrum 8	52.93	1.97		14.15	20.64	9.63			0.68		K-Feldspar
Spectrum 9	56.85			6.11	30.27	5.24	0.81		0.72		K-Feldspar
Spectrum 10	58.38				41.62						Quartz
Spectrum 11	49.66		0.57	3.36	7.77	2.13		35.20	1.31		Opaque
Spectrum 12	52.71			15.23	18.17	12.89			1.00		K-Feldspar
Spectrum 13	51.91		9.11		4.56		2.07		25.87	6.48	Mafic
Spectrum 14	51.58	2.41		15.57	21.38		9.06				Plagioclase
Spectrum 15	53.27		9.84		4.29		2.52		23.53	6.56	Mafic
Spectrum 16	53.82		10.33	3.37	4.79	0.98	1.70		25.02		Mafic
Spectrum 17	52.18	2.88		14.91	22.13		7.89				Plagioclase

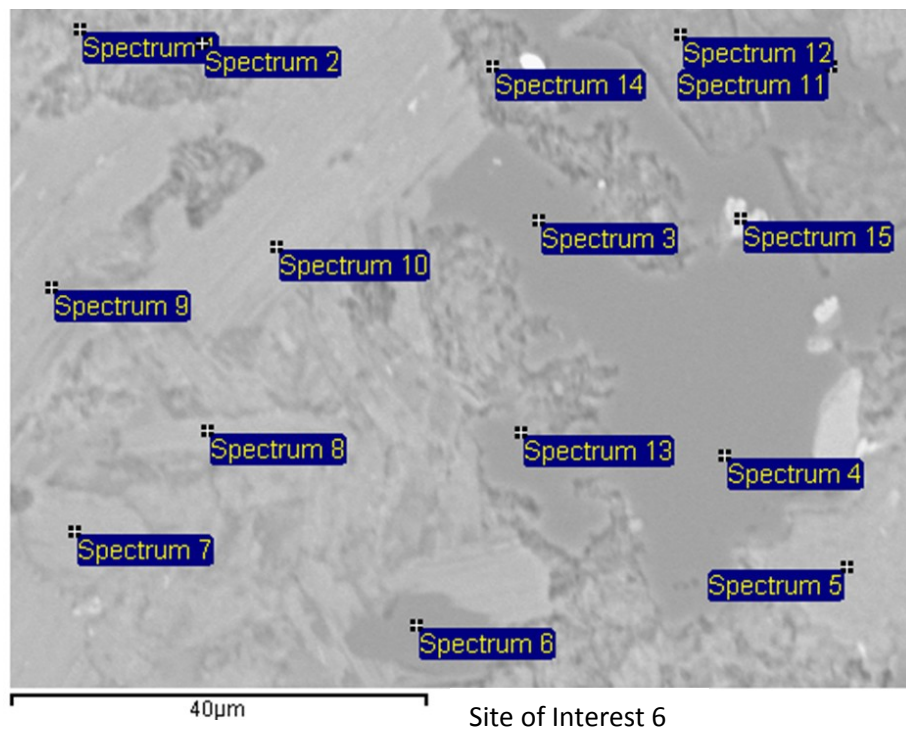
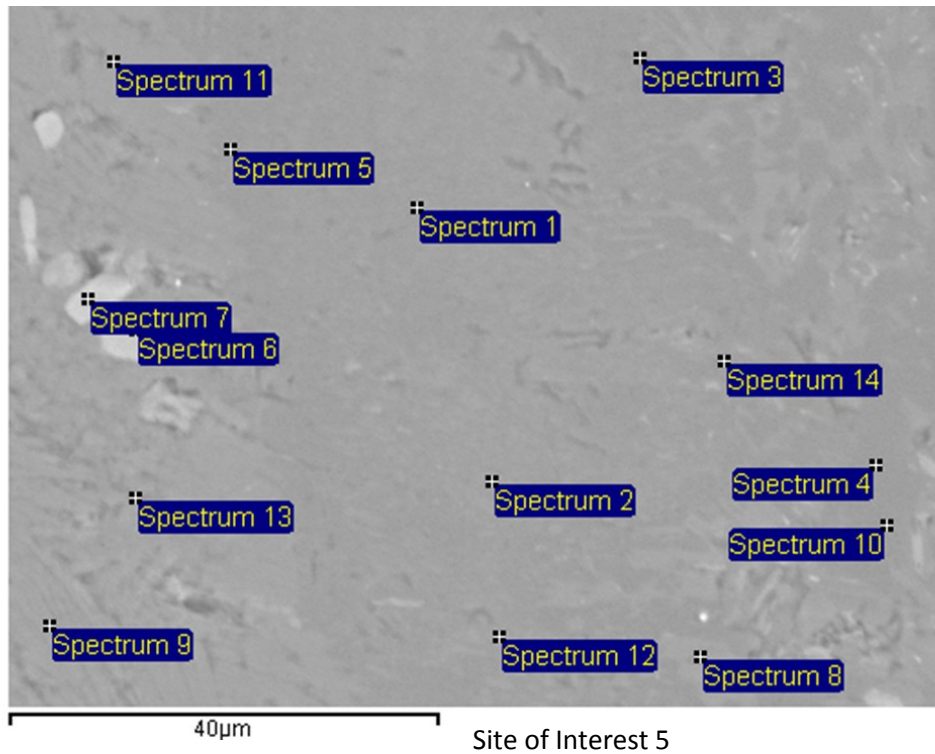
L02-02-139

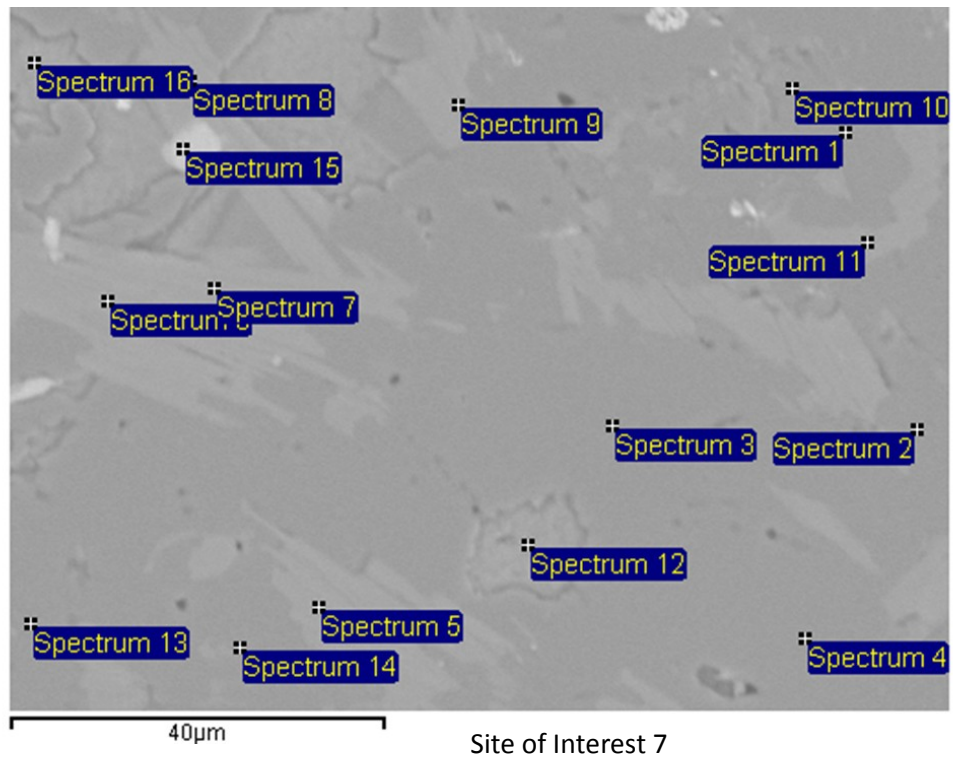


Site of Interest 1



Site of Interest 2





Site: Site of Interest 1

ID: LO2-02-139

	O	Mg	Al	Si	K	Ti	Mn	Fe	Hypothesized Phase
Spectrum 1	57.98			42.02					Quartz
Spectrum 2	51.35	6.83	10.85	10.57				20.40	Amphibole?
Spectrum 3	51.50	5.37	11.28	13.11	2.61			16.13	Amphibole?
Spectrum 4	50.90	6.88	10.82	10.71				20.69	Amphibole?
Spectrum 5	58.40			41.60					Quartz
Spectrum 6	57.47			41.84				0.69	Quartz
Spectrum 7	54.16	2.24	6.69	27.98	2.37	0.42		6.15	Mica?
Spectrum 8	52.92		14.52	17.56	13.34			1.65	K-Feldspar?
Spectrum 9	50.58	7.11	11.09	10.78			0.52	19.92	Amphibole?
Spectrum 10	51.28	6.36	10.78	11.62				19.95	Amphibole?
Spectrum 11	55.65	1.79	2.79	34.78	1.43			3.56	Amphibole?
Spectrum 12	58.07			41.93					Quartz

Site: Site of Interest 2

ID: LO2-02-139

	C	O	Na	Mg	Al	Si	Cl	K	Ti	Fe	Hypothesized Phase
Spectrum 1		50.10		7.07	11.17	11.04				20.63	?
Spectrum 2		58.03				41.97					Quartz
Spectrum 3		54.90	0.41		15.69	18.25		10.19		0.55	K-Feldspar
Spectrum 4		50.97			16.54	18.74		13.18		0.58	K-Feldspar
Spectrum 5		51.02		6.89	11.02	10.65				20.42	Amphibole?
Spectrum 6		57.88				42.12					Quartz
Spectrum 7		50.35		6.25	10.72	11.77				20.91	Amphibole?
Spectrum 8		54.84			11.61	20.45		8.68	2.95	1.47	K-Feldspar
Spectrum 9		48.73		4.95	12.03	13.71		2.45		18.13	Mica
Spectrum 10	35.14	35.10		2.06	5.49	6.79	0.81	0.81		13.80	Mica
Spectrum 11		50.48		5.63	11.45	12.10				20.34	Mafic

Site: Site of Interest 5

ID: LO2-02-139

	O	Na	Al	Si	P	K	Ca	Ti	V	Cr	Hypothesized Phase
Spectrum 1	57.28		5.02	33.13		4.12			0.46		?
Spectrum 2	56.09		5.96	32.46		4.90			0.60		?
Spectrum 3	56.13		2.05	39.95		1.49		0.39			K-Feldspar
Spectrum 4	58.26			41.74							Quartz
Spectrum 5	59.79			38.86		0.80		0.54			Quartz
Spectrum 6	46.18				16.78		37.04				Apatite
Spectrum 7	46.99				16.68		36.34				Apatite
Spectrum 8	54.09		10.07	26.96		8.00		0.44		0.44	Opaque
Spectrum 9	54.33		16.05	17.94		11.68					K-Feldspar
Spectrum 10	58.27			41.73							Quartz
Spectrum 11	55.09	0.45	15.28	18.05		10.63					K-Feldspar
Spectrum 12	56.60		7.36	29.71		5.82			0.51		K-Feldspar
Spectrum 13	52.89		15.26	19.59		10.94					K-Feldspar
Spectrum 14	57.47		2.65	36.80		1.49		0.53			K-Feldspar

Site: Site of Interest 6

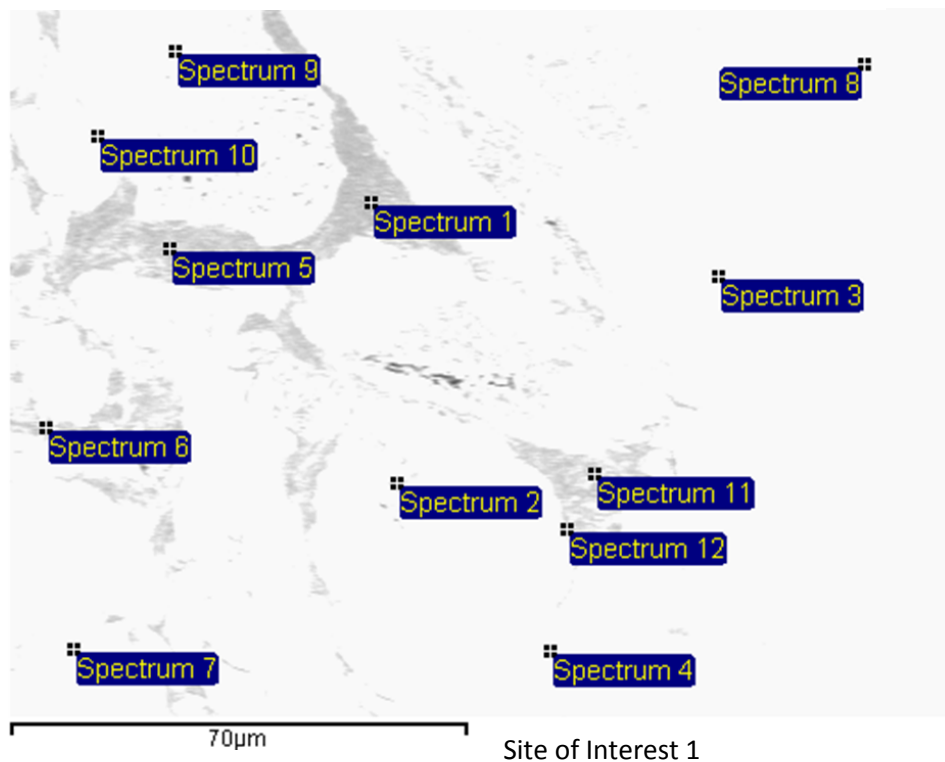
ID: LO2-02-139

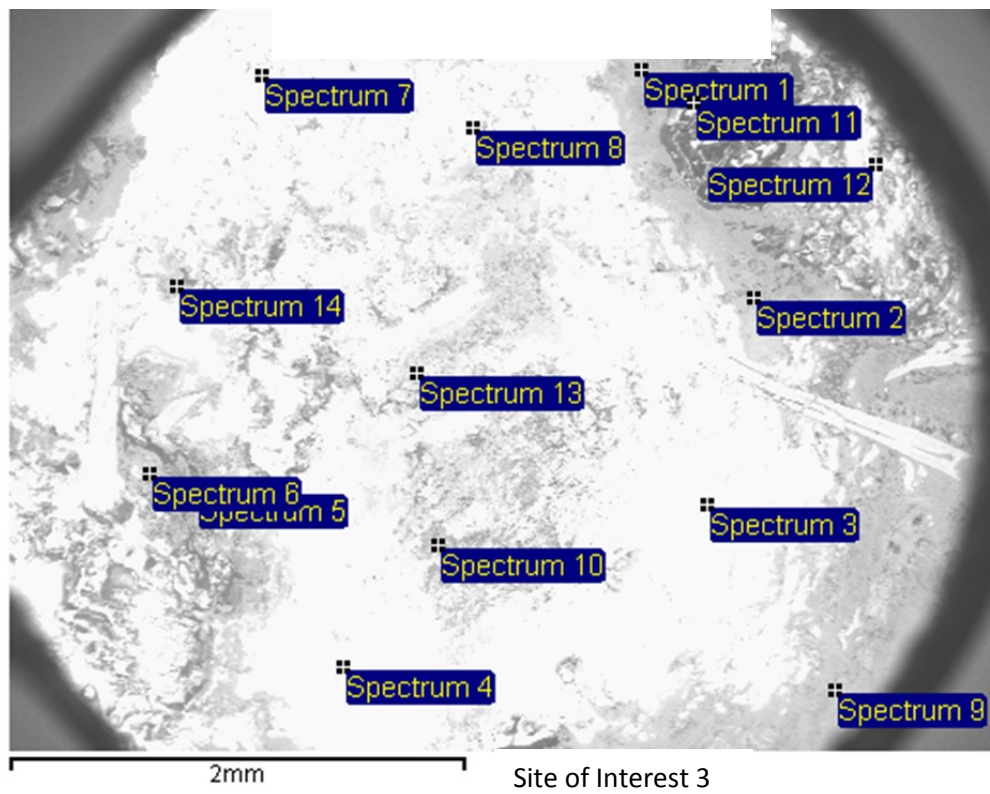
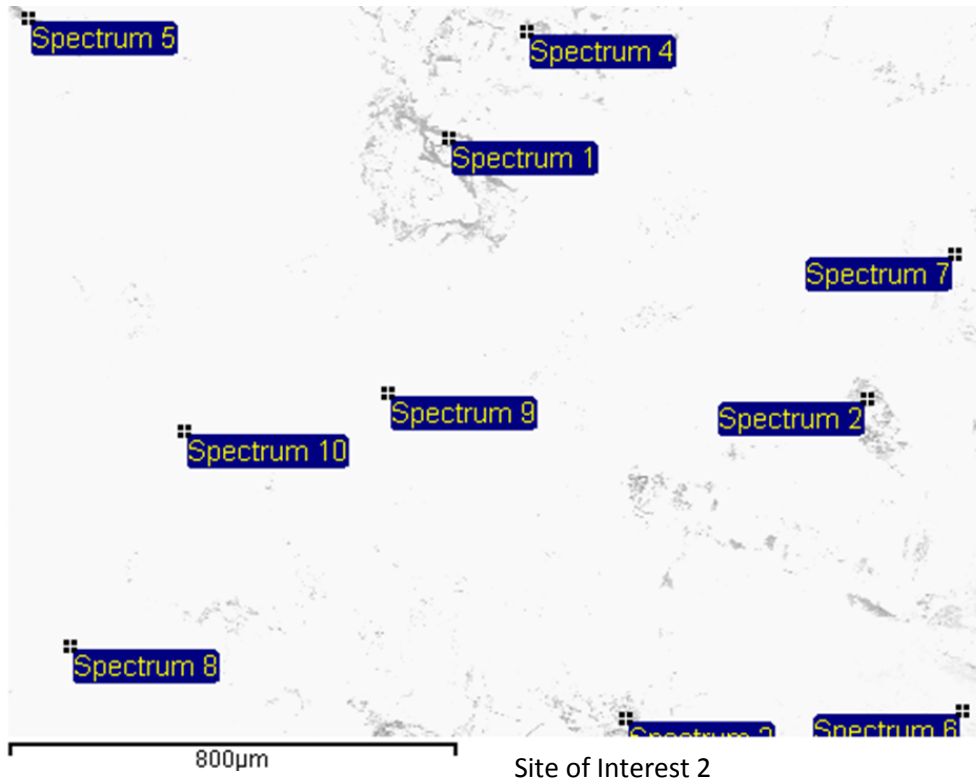
	O	Mg	Al	Si	Cl	K	Ti	Fe	Hypothesized Phase
Spectrum 1	49.69	4.79	10.88	12.77	0.66	0.77		20.43	Mica
Spectrum 2	48.83	5.02	11.04	13.70		0.73		20.69	Mica
Spectrum 3	59.29			40.71					Quartz
Spectrum 4	59.00			41.00					Quartz
Spectrum 5	52.19	6.32	11.07	10.83		1.35	0.70	17.54	Mica?
Spectrum 6	59.38			40.62					Quartz
Spectrum 7	52.79	7.04	10.10	11.45		1.49	0.75	16.38	Mica?
Spectrum 8	53.34	6.94	9.47	11.90		2.71	1.10	14.54	Mica?
Spectrum 9	55.63	2.41	10.62	16.50		9.27	1.46	4.10	Mica?
Spectrum 10	50.72	5.90	8.71	12.02		6.88	1.30	14.46	Mica?
Spectrum 11	58.96			41.04					Quartz
Spectrum 12	54.94		14.26	18.47		9.67		2.66	K-Feldspar
Spectrum 13	55.71	1.73	3.69	32.78				6.09	?
Spectrum 14	49.87	5.32	11.22	12.67	0.61			20.30	?
Spectrum 15			0.76	3.29			95.95		Opaque
Spectrum 16	48.98	5.47	10.92	12.65	0.69			21.29	Amphibole?
Spectrum 17	52.82	6.82	9.17	11.73		3.00	0.78	15.69	Mica?
Spectrum 18	52.81	7.10	10.33	11.58		1.03	0.61	16.54	Mica?
Spectrum 19	59.03			40.97					Quartz
Spectrum 20	52.73	7.40	11.62	10.39				17.86	Quartz

Site: Site of Interest 7
 ID: LO2-02-139

	O	Na	Al	Si	P	K	Ca	Ti	Fe	Zn	Hypothesized Phase
Spectrum 1	57.96			42.04							Quartz
Spectrum 2	58.25			41.75							Quartz
Spectrum 3	58.15			41.85							Quartz
Spectrum 4	58.17			40.91		0.92					Quartz
Spectrum 5	53.16		16.34	16.88		13.62					K-Feldspar
Spectrum 6	51.90		16.46	16.45		13.31		0.41	0.53	0.93	K-Feldspar
Spectrum 7	53.26	0.41	16.22	16.54		13.09		0.48			K-Feldspar
Spectrum 8	52.39	0.32	16.43	16.89		13.40			0.56		K-Feldspar
Spectrum 9	51.49		16.27	17.30		13.74		0.39		0.81	K-Feldspar
Spectrum 10	58.29			41.71							Quartz
Spectrum 11	52.92		16.22	16.94		13.29			0.63		K-Feldspar
Spectrum 12	52.44		16.46	17.51		13.59					K-Feldspar
Spectrum 13	58.24			41.76							Quartz
Spectrum 14	58.35			41.65							Quartz
Spectrum 15	46.27				16.68		37.05				Apatite
Spectrum 16	52.93		16.31	17.11		13.27		0.38			K-Feldspar

LO2-02-94





Site: Site of Interest 1

ID: L02-02-94

	C	O	Mg	Al	Si	K					Hypothesized Phase
Spectrum 1		79.08		8.53	10.83	1.56					K-Feldspar
Spectrum 2		82.17		8.20	9.62						Aluminium Silicate
Spectrum 3	32.31	61.93		2.46	3.30						?
Spectrum 4		77.58		9.42	11.47	1.53					K-Feldspar
Spectrum 5	46.60	47.66	1.50	1.32	2.91						?
Spectrum 6	78.99	18.73		1.09	1.19						Carbon Clasts
Spectrum 7	60.75	34.91	0.91	1.21	2.21						Carbon Clasts
Spectrum 8	29.91	67.91			2.18						Carbon Clasts
Spectrum 9	48.98	44.39	1.75	1.07	3.81						Carbon Clasts
Spectrum 10	45.04	48.48	1.37	1.91	3.20						Carbon Clasts
Spectrum 11	39.60	53.48			6.92						Carbon Clasts
Spectrum 12		78.59		8.82	10.97	1.62					K-Feldspar

Site: Site of Interest 2

ID: L02-02-94

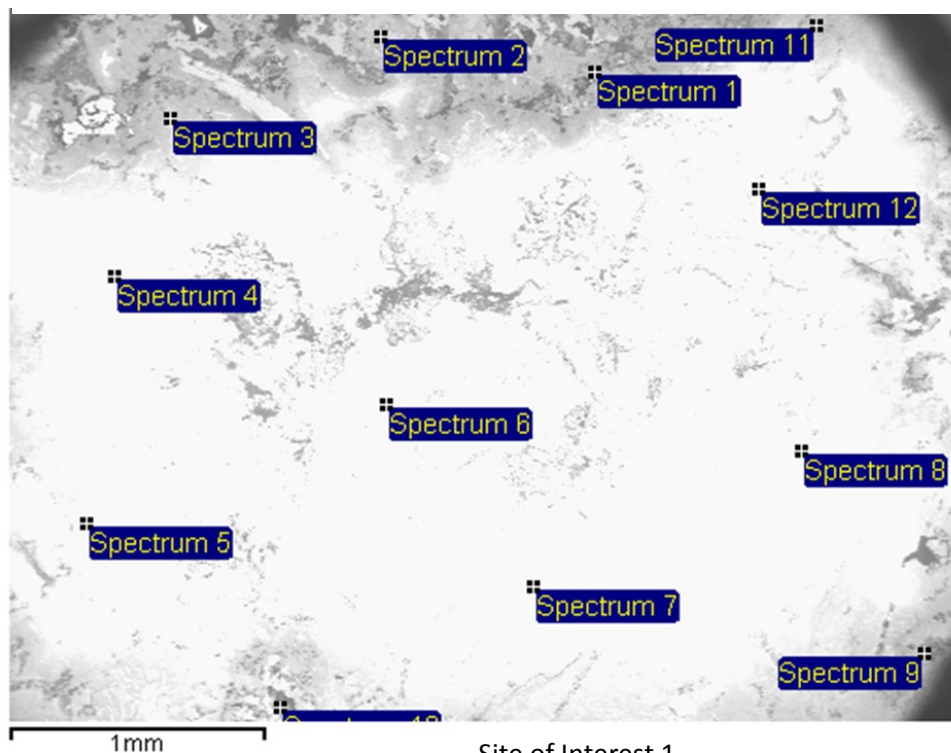
	C	O	Na	Mg	Al	Si	S	K	Ca	Fe	Hypothesized Phase
Spectrum 1	34.38	56.12		1.15	3.78	4.57					Carbon Clast
Spectrum 2		87.83				12.17					Quartz
Spectrum 3		84.98		1.56	3.91	9.55					Mg-Al Silicate
Spectrum 4	33.88	53.99	1.05		5.12	5.96					Feldspar
Spectrum 5	31.62	52.97	0.53	0.93	3.90	5.40	2.49		0.54	1.62	?
Spectrum 6	30.28	64.75			2.66	2.30					Aluminum Silicate
Spectrum 7	30.82	63.87			0.74	4.58					Aluminum Silicate
Spectrum 8		79.61			2.78	17.61					Aluminum Silicate
Spectrum 9		78.80		1.47	7.36	9.48	1.22	1.67			Mica
Spectrum 10		84.08	1.63		6.20	8.10					Feldspar

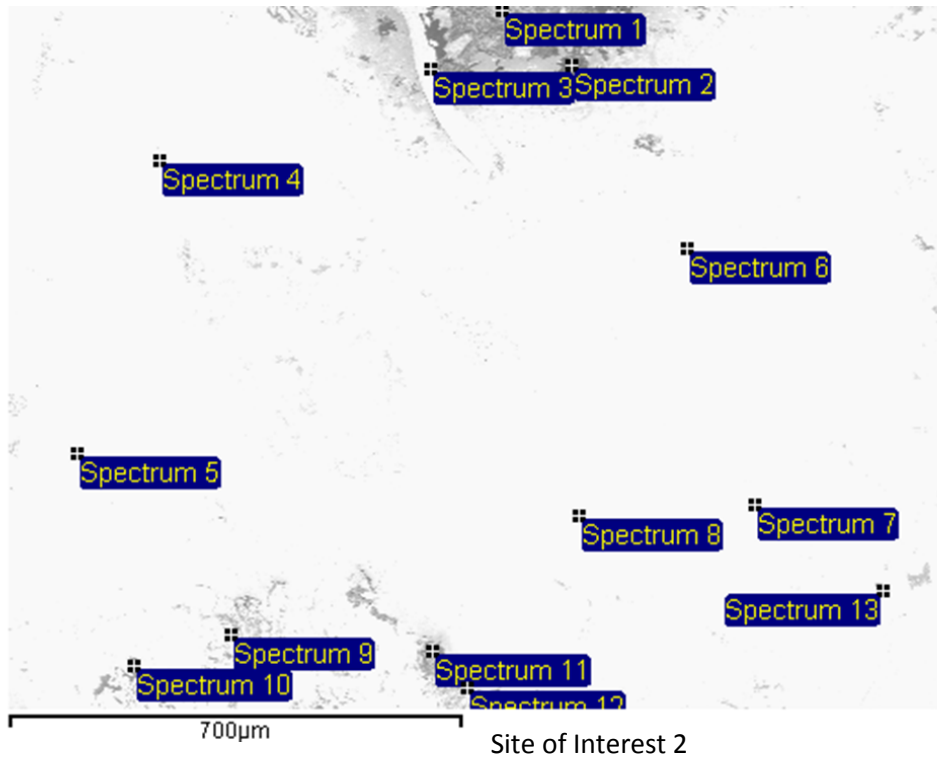
Site: Site of Interest 3

ID: L02-02-94

	C	O	Na	Mg	Al	Si	Cl	K	Fe	Hypothesized Phase
Spectrum 1		74.89	2.30		10.80	12.00				Plagioclase
Spectrum 2		85.38			2.89	11.73				Quartz
Spectrum 3	31.64	56.37		1.13	4.17	5.45		0.53	0.70	Quartz
Spectrum 4		73.33			2.81	23.86				Quartz
Spectrum 5	49.41	40.49			3.24	5.63		1.23		K-Feldspar
Spectrum 6	41.33	47.65		0.99	3.47	5.06	0.21	1.29		K-Feldspar
Spectrum 7		70.10			3.15	25.12		1.63		K-Feldspar
Spectrum 8		79.02			10.29	10.68				Quartz
Spectrum 9		82.70	1.86		8.34	7.10				Plagioclase
Spectrum 10	38.58	49.60	0.77	1.01	3.95	5.68		0.41		Mica
Spectrum 11	62.99	33.58			1.40	2.02				Quartz
Spectrum 12		71.73				28.27				Quartz
Spectrum 13		90.15			3.90	5.95				Aluminum Silicate
Spectrum 14	30.35	58.72	0.54		2.85	7.55				?

L02-02-79





Site: Site of Interest 1
 ID: L02-02-79

	C	O	Na	Mg	Al	Si	Cl	K	Ti	Fe	Hypothesized Phase
Spectrum 1	54.90	32.46	0.39		4.63	5.57		1.03		1.02	Carbon Clast
Spectrum 2	39.41	48.99				11.36	0.24				Carbon Clast
Spectrum 3		72.93				24.19			2.88		Quartz
Spectrum 4		87.03				12.97					Quartz
Spectrum 5		85.54			7.40	7.06					Aluminum Silicate
Spectrum 6		97.65				2.35					Quartz
Spectrum 7		91.60			2.09	6.31					Aluminum Silicate
Spectrum 8		97.32				2.68					Quartz
Spectrum 9		84.62				15.38					Quartz
Spectrum 10		97.87				2.13					Quartz
Spectrum 11		100.00									?
Spectrum 12		91.79			2.03	6.18					Aluminum Silicate
Spectrum 13		84.15		1.78	7.33	6.73					?

Site: Site of Interest 2

ID: L02-02-79

	C	O	Mg	Al	Si	K	Hypothesized Phase
Spectrum 1		71.69		3.87	22.70	1.75	K-Feldspar
Spectrum 2		75.15	3.27	5.67	15.90		?
Spectrum 3		82.92		8.70	8.38		Aluminum Silicate
Spectrum 4		92.80		2.69	4.51		Aluminum Silicate
Spectrum 5		92.75		3.72	3.53		Aluminum Silicate
Spectrum 6	35.51	62.98		0.79	0.72		Carbon Clast
Spectrum 7		95.71			4.29		Quartz
Spectrum 8		92.08			7.92		Quartz
Spectrum 9		78.87		6.17	14.96		Aluminum Silicate
Spectrum 10		76.26	4.61	8.12	11.01		Aluminum Silicate
Spectrum 11		84.87		6.68	8.46		Aluminum Silicate
Spectrum 12	39.63	49.51		2.23	8.10	0.53	K-Feldspar?
